



Extent, thickness and erosion of the Jurassic continental flood basalts of Dronning Maud Land, East Antarctica: A low-T thermochronological approach

Sirevaag Hallgeir ^{a,*}, Jacobs Joachim ^{a,b}, Ksienzyk Anna K. ^a, Dunkl István ^c, Marschall Horst R. ^d

^a Department of Earth Science, University of Bergen, PB 7803, N-5020 Bergen, Norway

^b Norwegian Polar Institute, Fram Centre, PB 6606 Langnes, N-9296 Tromsø, Norway

^c Geoscience Centre, University of Göttingen, Goldschmidtstraße 3, D-37077 Göttingen, Germany

^d Institut für Geowissenschaften, Goethe Universität Frankfurt, Altenhöferallee 1, D-60438 Frankfurt am Main, Germany

ARTICLE INFO

Article history:

Received 24 October 2017

Received in revised form 9 April 2018

Accepted 27 April 2018

Available online 08 June 2018

Handling Editor: T. Tsunogae

Keywords:

Apatite fission track

(U–Th)/He

Thermal modelling

Passive margin

Gondwana rifting

ABSTRACT

The Dronning Maud Land Mountains form a c. 1500 km long, coast-parallel escarpment that possibly formed by flexural uplift during Jurassic rifting between East and West Gondwana. Contemporaneous to the rifting, considerable amounts of continental flood basalts, associated with the Karoo mantle plume, were emplaced at c. 183 Ma. The basalts are still widespread in South Africa, making up elevated topography, but are only preserved as smaller remnants in western Dronning Maud Land. By investigating the paleo-thermal effect of the basalts, we aim to constrain the extent and original thickness, as well as the subsequent erosion history of the Jurassic continental flood basalts. Thus, we have applied low-temperature thermochronological methods to 40 samples from western Dronning Maud Land. This has resulted in 34 new apatite fission track ages, ranging from c. 310 to 90 Ma, 31 apatite (U–Th)/He ages spanning from c. 400 to 50 Ma and, and 9 zircon (U–Th)/He ages between c. 650 and 200 Ma.

Thermal modelling of 26 samples indicates variable thickness of the Jurassic basaltic cover. The greatest basaltic thicknesses are recorded in Heimefrontfjella and H.U. Sverdrupfjella, where up to c. 2 km are estimated. Thicknesses at Kirwanveggen, Hochlinfjellet, Midbresrabben and Ahlmannryggen range from c. 100 m to 600 m. Thickness variations are attributed to the proximity to the emplacement zone, possible pre-existing topography and syn-volcanic rift flank uplift.

Since the continental flood basalt emplacement, two phases of enhanced cooling have been documented: 1) A Jurassic–Cretaceous cooling phase is attributed to reactivation of the Jutulstraumen–Penckgraben rift, the initial rifting and opening of the South Atlantic and enhanced chemical weathering and deep erosion due to a Jurassic temperate–subtropical climate. 2) Late Paleogene cooling is attributed to the transition from green house to ice-house conditions and ice-sheet initiation at the Eocene–Oligocene boundary. Post-Jurassic denudation of at least 2 km in some places is suggested.

© 2018 International Association for Gondwana Research. Published by Elsevier B.V. All rights reserved.

1. Introduction

The Dronning Maud Land (DML) Mountains, East Antarctica, form a c. 1500 km long, largely coast-parallel mountain range that stretches from Sør Rondane in the east, to H.U. Sverdrupfjella in the west and Heimefrontfjella in the southwest. The crest of the mountain range is located c. 200 km inland from the coastline. In the DML Mountains, Jurassic basaltic lava flows and sills are exposed in isolated outcrops throughout western Dronning Maud Land (Furnes et al., 1987; Harris

et al., 1990; Jacobs et al., 1996a; Luttinen and Furnes, 2000; Luttinen et al., 2015; Figs. 1, 2). These basalts are considered to be part of the once widespread continental flood basalt province that is associated with the Karoo mantle plume and was emplaced at c. 183 Ma during the Early Jurassic rifting between East and West Gondwana (Duncan et al., 1997; Luttinen and Furnes, 2000; Riley and Knight, 2001; Jourdan et al., 2007; Svensen et al., 2012; Fig. 1). While the scattered outcrops of Jurassic basalt in DML are merely small erosional remnants of this flood basalt province, basalts of similar age are still widespread in South Africa, where the corresponding Sabie River Basalt Formation of the Lebombo Monocline is preserved in thicknesses up to c. 5 km (e.g. Cleverly and Bristow, 1979; Luttinen and Furnes, 2000; Riley et al.,

* Corresponding author.

E-mail address: Hallgeir.Sirevaag@gmail.com (H. Sirevaag).

2004). Based on the present-day extent and thickness of the Jurassic basalts on the conjugate margin in southern Africa, it is likely that the basalts once were similarly thick and widespread in Dronning Maud Land.

Constraining the extent and thickness of the Jurassic continental flood basalt province on both conjugate margins is of great value for geodynamic reconstructions, since it can provide new insights into the geometry of the rift system prior to the onset of Gondwana breakup. The extent, thickness and especially the erosional history of the basalts is further critical for reconstructing the post-Jurassic landscape development of DML. Were the thick layers of basalt eroded quickly during Jurassic rifting or more slowly during the continuous evolution of the passive margin in the Cretaceous? Or were they resisting erosion until the Cenozoic glaciation? If significant parts of the thick basaltic cover prevailed until they were stripped by the early Antarctic ice-sheets at the onset of glaciation at 34 Ma (e.g. DeConto and Pollard, 2003), the extra basaltic overburden would make a significant difference to the

pre-glacial landscape and is therefore highly relevant for future studies investigating the early glaciation history of Antarctica.

Previous thermochronological work trying to estimate the thickness of the Jurassic continental flood basalts is restricted to Heimefrontfjella in southwestern DML (Fig. 2). Based on apatite fission track (AFT) data, Jacobs and Lisker (1999) suggested that up to 2 km of Jurassic basalts were emplaced, and later mostly eroded in Heimefrontfjella. Here we apply this approach to a much larger area, covering all of western DML in an attempt to define the eastern extent of the continental flood basalts. Additionally, low-temperature thermochronological methods have significantly evolved during the last two decades, and we combine different thermochronometers that allow us to cover a wider range of temperatures (c. 35–230 °C; Farley and Stockli, 2002; Reiners et al., 2002); altogether, this allows for much more detailed *t*–*T* modelling. In this contribution, we present apatite fission track and apatite and zircon (U-Th)/He (AHe, ZHe) data from 40 samples that provide new insights into the thickness and geographic distribution of the

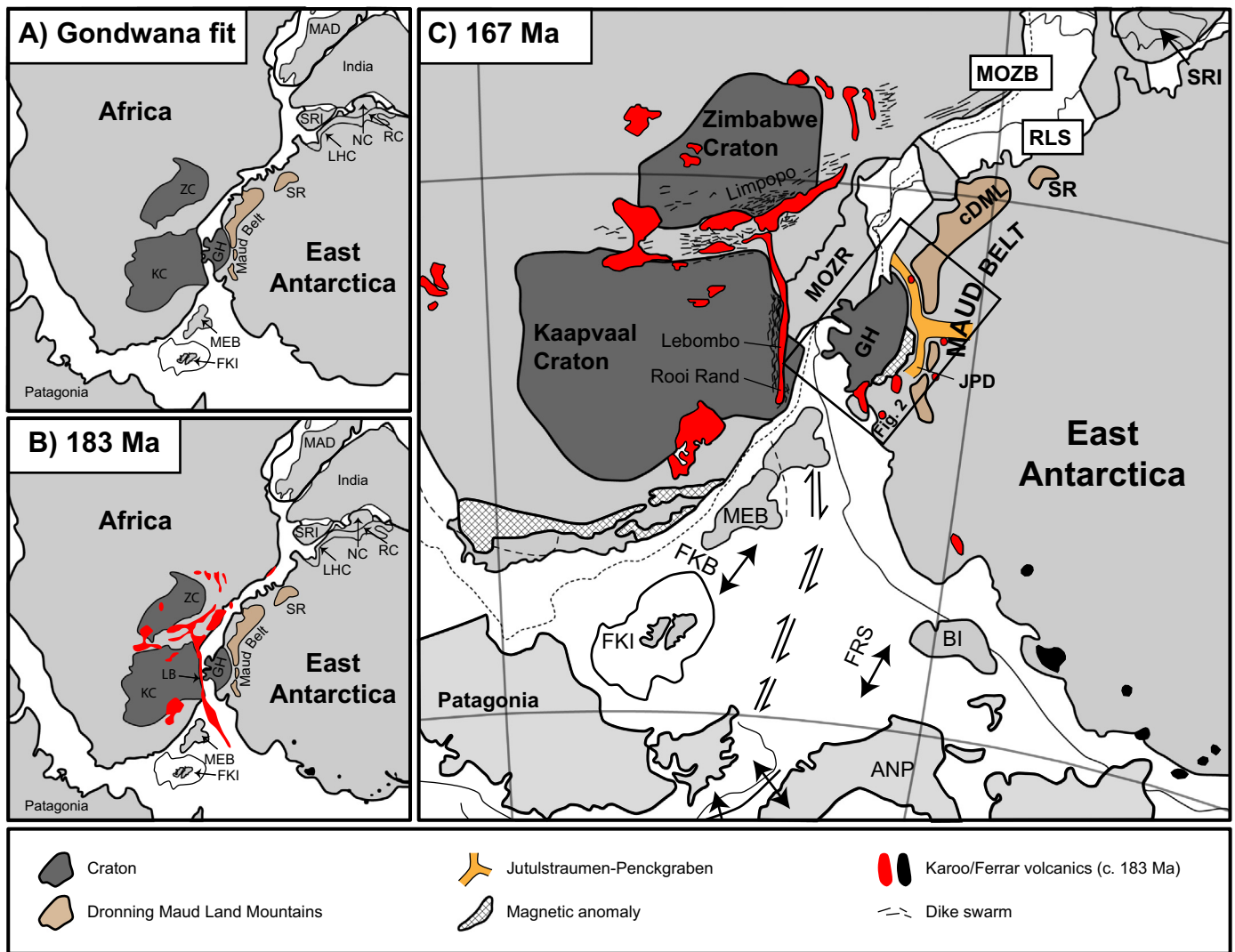


Fig. 1. Gondwana reconstruction from pre-rift to rift phase. A) Gondwana-fit prior to continental flood basalt emplacement, showing that the Grunehogna Craton forms the Antarctic counterpart of the Kaapvaal Craton. B) Early Jurassic reconstruction, indicating the initial phase of continental flood basalt emplacement. C) Gondwana reconstruction after emplacement of Jurassic continental flood basalts. The continental flood basalts are widespread in south-east Africa, while they are only preserved in scattered outcrops in Dronning Maud Land. A and B are modified after [Leinweber and Jokat \(2012\)](#) and [Dalziel et al. \(2013\)](#), C is modified after [König and Jokat \(2006\)](#), [Dalziel et al. \(2013\)](#), [Cox \(1992\)](#) and [Luttinen et al. \(1998\)](#). Abbreviations: ANP – Antarctic Peninsula; BI – Berkner Island; cDML – central Dronning Maud Land; FKB – Falkland Plateau Basin; FKI – Falkland Islands; FRS – Filchner-Ronne Shelf; GH – Grunehogna Craton; JPD – Jutulstraumen–Penckgraben discontinuity; KC – Kaapvaal Craton; LB – Lebombo; LHC – Lützow-Holm Complex; MAD – Madagascar; MEB – Maurice Ewing Bank; MOZB – Mozambique Basin; MOZR – Mozambique Ridge; NC – Napier Complex; RC – Rayner Complex; RLS – Riiser-Larsen Sea; SR – Sor Rondane; SRI – Sri Lanka; ZC – Zimbabwe Craton.

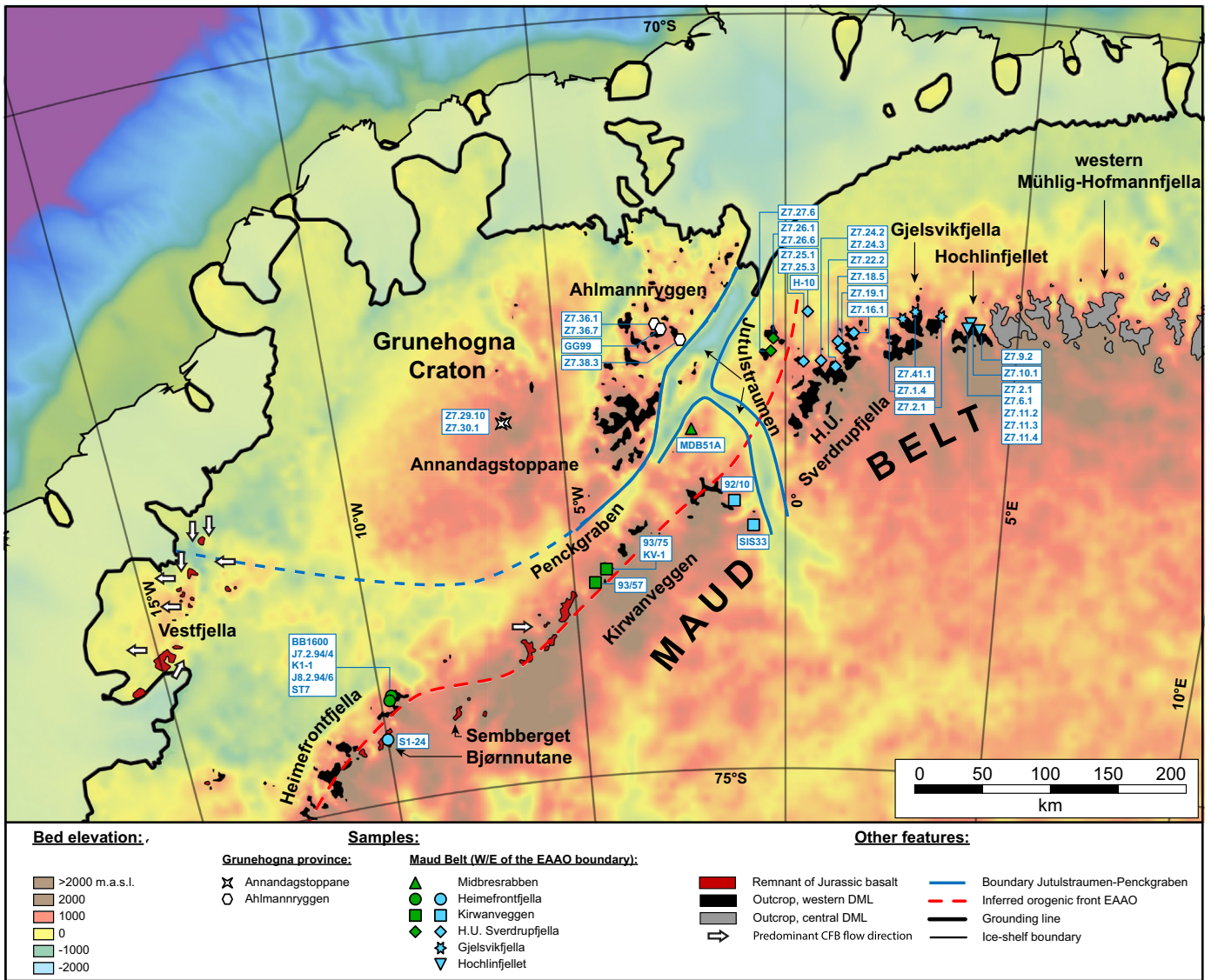


Fig. 2. Sub-ice topography of western Dronning Maud Land after BEDMAP2 (Fretwell et al., 2013), and the present-day distribution of the Jurassic continental flood basalts. Samples have been obtained from three distinct geological provinces: (1) from the Grunehogna Province (white symbols), (2) from the non-overprinted part of the Mesoproterozoic Maud Belt (green symbols), and (3) from the part of the Maud Belt that was overprinted by the Pan-African East African–Antarctic Orogeny (blue symbols). (For interpretation of the references to colour in this figure legend, the reader is referred to the web version of this article.)

Continental flood basalt localities and flow directions are from Harris et al. (1990), Luttinen and Furnes (2000), Luttinen et al. (2010) and Spaeth (2009) and Luttinen et al. (2010).

Jurassic continental flood basalts in western Dronning Maud Land and their subsequent erosion.

2. Geological setting of western Dronning Maud Land

Western Dronning Maud Land comprises two main geological provinces: the Archean Grunehogna Craton and the Mesoproterozoic Maud Belt, separated by the major Jutulstraumen–Penckgraben discontinuity (Figs. 1, 2). Gondwana reconstructions commonly place western DML adjacent to SE Africa (e.g. Smith and Hallam, 1970; Martin and Hartnady, 1986; Groenewald et al., 1991; Moyes et al., 1993; Groenewald et al., 1995; Jacobs et al., 1998; König and Jokat, 2006; Jacobs et al., 2008; Leinweber and Jokat, 2012; Fig. 1), with the Grunehogna Craton forming the Antarctic counterpart of the Archean Kaapvaal Craton, and the Maud Belt representing the link to the Mesoproterozoic Namaqua–Natal Belt and Mozambique Belt (e.g. Arndt et al., 1991; Thomas et al., 1994; Wareham et al., 1998; Jacobs et al., 1993; Jacobs et al., 2003b; Jacobs et al., 2008).

Basement outcrops of the Grunehogna Craton are restricted to the c. 3.1 Ga Annandagstoppane granite (Barton et al., 1987; Marschall et al., 2010). Additionally, the c. 1130–1108 Ma volcanoclastic Ritscherflya Supergroup is exposed at Ahlmannryggen and Borgmassivet in thicknesses up to c. 2000 m, covering the Archean basement (Wolmarans and Kent, 1982; Perritt, 2001; Marschall et al., 2013). The Maud Belt surrounds the Grunehogna Craton on its southern and eastern sides and stretches from Heimefrontfjella in the SW towards Mühlig-Hofmannfjella in the NE (Fig. 2). Grenville-age (1090–1060 Ma) amphibolite- to granulite-facies meta-sedimentary and meta-igneous rocks, related to the assembly of Rodinia, form the basement of the Maud Belt (e.g. Arndt et al., 1991; Jacobs et al., 2003b). Parts of the Maud Belt show a Pan-African (c. 590–490 Ma) tectono-thermal overprint related to the East African–Antarctic Orogen (EAAO) and the assembly of Gondwana (Moyes et al., 1993; Groenewald et al., 1995; Jacobs et al., 1996a; Jacobs et al., 2003a; Jacobs et al., 2003c; Jacobs and Thomas, 2004; Board et al., 2005; Bisnath et al., 2006; Pauly et al., 2016; Fig. 2). In Heimefrontfjella, this is documented by biotite and muscovite K–Ar and ^{40}Ar – ^{39}Ar ages of c. 535–470 Ma. The boundary

between the overprinted and non-overprinted regions of the Maud Belt corresponds to the 20 km wide transpressive, dextral Heimefront Shear Zone (e.g. Jacobs et al., 1995; Golynsky and Jacobs, 2001; Bauer et al., 2016), which is interpreted as the western orogenic front of the East African–Antarctic Orogen (EAAO), and possibly related to lateral escape tectonics (Jacobs and Thomas, 2004).

In Heimefrontfjella, Kirwanveggen and Fossilryggen, the Mesoproterozoic basement is unconformably overlain by up to c. 160 m of Late Carboniferous–Middle Permian Beacon sedimentary rocks (Plumstead, 1975; Olausen, 1985; Lindström, 1995a, 1995b; Bauer, 2009). The unconformity forms a distinct peneplain exposed at c. 2100 masl in Heimefrontfjella and Kirwanveggen, indicating that the presently exposed basement was already once close to the surface during Permian times. This peneplain can be traced over large distances. At Jutulessen, western Mühlig-Hofmannfjella (Fig. 2), relicts of an Early Permian paleosurface exposed at a similar elevation have been interpreted to represent the same peneplain and that the Beacon sediments were deposited on in Heimefrontfjella and Kirwanveggen, >500 km away (Näslund, 2001). Also, within the Transantarctic Mountains, along the tectonic boundary between East and West Antarctica, a similar peneplain has been identified as the Kukri erosional surface. This surface separates the Cambro-Ordovician basement from the overlying Beacon sediments. However, within the Transantarctic Mountains the preserved section of Beacon sediments is much more complete than in Dronning Maud Land, amounting to 2.5–3 km of Devonian to Triassic siliciclastic sediments (McKelvey et al., 1977; Barrett, 1981; Isbell, 1999). Comparing this thick sedimentary sequence to the mere 160 m of Beacon sediments at Fossilryggen, it is likely that the Beacon sediments of western Dronning Maud Land were considerably thicker than what is preserved today. Significant pre-Jurassic erosion of the Beacon sediments has been documented at Bjørnnutane in Heimefrontfjella (Fig. 2), where only 2 m of vitrified sandstone separate the crystalline basement from the Jurassic continental flood basalts (Jukes, 1972; Bauer, 2009).

2.1. Jurassic magmatism in western Dronning Maud Land

In western Dronning Maud Land, Jurassic continental flood basaltic lavas and sills are exposed in variable thicknesses in Vestfjella (c. 400–>1000 m; Luttinen and Furnes, 2000; Luttinen et al., 2015), southern Kirwanveggen (c. 400 m; Furnes et al., 1987; Harris et al., 1990), Sembberget (c. 250–300 m; Jacobs et al., 1996b; Luttinen et al., 2010), Bjørnnutane (c. 200 m; Luttinen et al., 2010) and Heimefrontfjella (c. 100–200 m; Jacobs et al., 1996b; Luttinen et al., 2010) (Fig. 2). Where the base of the continental flood basalts is exposed, they overlie Beacon sedimentary rocks (e.g. Jacobs et al., 1996b; Luttinen and Furnes, 2000; Zhang et al., 2003). Whereas intrusive equivalents (sills and dikes) of the flood basalts are rare in Heimefrontfjella and Kirwanveggen, they are abundant in H.U. Sverdrupfjella, Ahlmannryggen and Vestfjella (e.g. Furnes and Mitchell, 1978; Riley et al., 2005; Curtis et al., 2008).

Plagioclase K–Ar and ^{40}Ar – ^{39}Ar analyses of the Vestfjella and Kirwanveggen lavas yielded ages of 180–185 Ma (e.g. Duncan et al., 1997). The age of the Vestfjella and Kirwanveggen lavas corresponds well to the c. 183 Ma age of the basalts of Lesotho and Lebombo in southeast Africa (Duncan et al., 1997). During Early Jurassic times, western Dronning Maud Land was located adjacent to the Lebombo Monocline in southeastern Africa (Martin and Hartnady, 1986; Harris et al., 1990; Cox, 1992; Luttinen and Furnes, 2000; König and Jokat, 2006; Leinweber and Jokat, 2012; Fig. 1B). This is also confirmed by the geochemical resemblance between the Dronning Maud Land lavas and the Karoo magmatism of the Lebombo Monocline (e.g. Harris et al., 1990; Luttinen and Siivola, 1997; Luttinen and Furnes, 2000). It has been suggested that the continental flood basalts of western DML were partly emplaced through both the Jutulstraumen–Penckgraben and Mozambique–Weddell Sea lithospheric thinning zones, similar to the Lebombo basalts (Luttinen and Furnes, 2000). The flow directions

of the lavas vary regionally, with an eastward flow recorded in Kirwanveggen, while southward, northward and westward flow directions are recorded in northern, southern and central Vestfjella, respectively (Harris et al., 1990; Luttinen and Furnes, 2000; Fig. 2).

3. Previous thermochronology from Dronning Maud Land

In western Dronning Maud Land, previous thermochronological studies are restricted to Heimefrontfjella, Gjelsvikfjella and western Mühlig-Hofmannfjella. Vitritite reflectance data of c. 0.5% from coal seams in Permian sediments in Heimefrontfjella indicate maximum temperatures of 70–80 °C since the Permian (Bauer et al., 1997). In Heimefrontfjella and Mannefallknausane, 37 Middle Jurassic–Late Cretaceous AFT ages all postdate the continental flood basalts, and are thus interpreted to have suffered complete annealing under 1.5–2 km of basalt, corresponding to temperatures of c. 80–130 °C. Since the fission tracks were completely annealed, but the coal seams were not significantly matured, Jacobs and Lisker (1999) suggested that a short-lived Jurassic thermal event might reconcile these different temperature estimates. The Jurassic reheating was then followed by rapid exhumation during mid-Cretaceous times (Jacobs et al., 1995; Jacobs and Lisker, 1999). Early Cretaceous–Eocene single-grain apatite (U–Th)/He ages from four of these samples document slow cooling until Cenozoic times, before accelerated cooling interpreted as flexural isostatic rebound and differential exhumation in response to the load of the developing ice shield (Emmel et al., 2008).

In Gjelsvikfjella and western Mühlig-Hofmannfjella, thirteen Late Devonian–Early Jurassic AFT ages and four Cambrian–Middle Carboniferous titanite fission track (TFT) ages document two cooling steps, with the main cooling prior to the Jurassic passive margin evolution and a second Late Cretaceous cooling phase. As opposed to Heimefrontfjella, no reheating due to the continental flood basalts was reported (Emmel et al., 2009).

East of our study area, the post-Pan-African thermal evolution of central Dronning Maud Land has been investigated by 126 apatite, 19 titanite and 14 zircon fission track ages, mainly derived from basement rocks (Meier, 1999; Meier et al., 2004; Emmel et al., 2007). The AFT ages range from Middle Carboniferous to Late Cretaceous, however Early–Middle Jurassic ages are clearly predominant (Meier, 1999; Meier et al., 2004; Emmel et al., 2007). Most of the titanite fission track ages range from Late Ordovician to Early Permian (Meier, 1999), while the zircon fission track ages scatter between Late Devonian and the Middle Triassic (Meier, 1999; Meier et al., 2004). Additionally, Emmel et al. (2007) reported Late Carboniferous–Middle Cretaceous single-grain AHe ages from central DML. The combined dataset documents the thermal evolution since the Pan-African Orogeny, indicating slow post-orogenic cooling until the Triassic (Meier, 1999; Meier et al., 2004), possibly with a phase of accelerated cooling during the Carboniferous (Emmel et al., 2007). Since Early Jurassic times, phases of accelerated cooling have been attributed to the initial Gondwana rifting and passive margin evolution (Early Jurassic), opening of the Riiser-Larsen Sea and detachment of India from Antarctica (Late Jurassic) and accelerated northward drift of India (Middle Cretaceous) (e.g. Meier, 1999).

4. Samples and analytical methods

The present study includes 40 samples, predominantly from basement rocks of western Dronning Maud Land (Table 1, Fig. 2). Two samples, J8.2.94/6 and ST7, are granite clasts from the base of the Permian–Carboniferous Beacon sediments in Heimefrontfjella, and thus overly the basement; two samples, Z7.26.1 and SIS33, come from the Jurassic syenite intrusions of Straumsvola and Siste fjell, respectively. The samples were collected at elevations between c. 930 and 2325 masl within the Maud Belt, Jutulstraumen area and the Grunehogna Craton. The samples were chosen according to locality and elevation to ensure a representative dataset to spatially cover the entire region. Apatite and

Table 1
List of analyzed samples.

Sample	Lithology	Locality	Region	Coordinates		Elevation	Analyses	
				Latitude	Longitude			
Grunehogna Province								
Z7.29.10	Cumulate	Annandagstoppane	Grunehogna	−72.6036	−6.2130	1870	AFT	AHe
Z7.30.1	Cumulate	Annandagstoppane	Grunehogna	−72.6092	−6.3093	1670	AFT	AHe
Z7.36.1	Diorite	Ahlmannryggen	Grunehogna	−72.0386	−2.8019	1130	AFT	AHe
Z7.36.7	Diorite	Ahlmannryggen	Grunehogna	−72.0293	−2.8067	975	AFT	
Z7.38.3	Sandstone/greywacke	Ahlmannryggen	Grunehogna	−72.1407	−2.2710	1080		AHe
GG99	Gabbro	Ahlmannryggen	Grunehogna	−72.0645	−2.6790	1395	AFT	AHe
Maud Belt - West of EAAO								
J7.2.94/4	Trondhjemitite	Buråsbotnen	Heimefrontfjella	−74.3000	−9.7333	1300	AFT	AHe
BB1600	Granitic orthogneiss	Buråsbotnen	Heimefrontfjella	−74.3000	−9.7333	1600	AFT	AHe
J8.2.94/6	Granite dropstone	Schivestolen	Heimefrontfjella	−74.3000	−9.7333	2100	AFT	AHe ZHe
ST7	Granite dropstone	Schivestolen	Heimefrontfjella	−74.3000	−9.7333	2100	AFT	AHe
K1-1	Tonalitic gneiss	Kottasberge/Milorgfjella	Heimefrontfjella	−74.3000	−9.7333	1600		ZHe
KV-1	Augen gneiss	Enden	Kirwanveggen	−73.6340	−4.2175	2020		ZHe
93/75	Augen gneiss	Enden	Kirwanveggen	−73.2167	−4.5500	2000	AFT	
93/57	Augen gneiss	Skappelnabben	Kirwanveggen	−73.2167	−4.5500	2250	AFT	AHe ZHe
MDB50	Tonalite/granodiorite	Midbresrabben	Jutulstraumen	−72.7333	−2.1000	1530		AHe ZHe
MDB51A	Tonalite/granodiorite	Midbresrabben	Jutulstraumen	−72.7333	−2.1000	1530	AFT	AHe
Z7.26.1	Syenite	Straumsvola	H.U. Sverdrupfjella	−72.1384	−0.2788	1270	AFT	AHe
Z7.26.6	Gneiss	Straumsvola	H.U. Sverdrupfjella	−72.1444	−0.2561	1245	AFT	
Z7.27.6	Metavolcanic gneiss	Brekkerista	H.U. Sverdrupfjella	−72.2282	−0.3126	930	AFT	AHe
Maud Belt - EAAO								
S1-24	Grt-rich augen gneiss	Northern XU-fjella	Heimefrontfjella	−74.3000	−9.7333	1300		ZHe
92/10	Augen gneiss	Neumayerskarvet	Kirwanveggen	−73.2167	−1.1667	2100	AFT	AHe
SIS33	Syenite	Sistefjell	Kirwanveggen	−73.3830	−0.7333	2325		AHe
H-10	Tonalite/granodiorite	Holane	H.U. Sverdrupfjella	−71.9667	0.4833	1000	AFT	AHe ZHe
Z7.16.1	Syenite	Brattskarvet	H.U. Sverdrupfjella	−72.1025	1.4792	1435	AFT	AHe
Z7.18.5	Paragneiss	Rømlingane	H.U. Sverdrupfjella	−72.1605	1.1392	1475	AFT	
Z7.19.1	Migmatite	Vendeholten	H.U. Sverdrupfjella	−72.2075	1.2298	1510	AFT	AHe
Z7.22.2	Grt-bearing layered gneiss	Isingen	H.U. Sverdrupfjella	−72.3288	1.0990	1785	AFT	AHe
Z7.24.2	Felsic gneiss	Fuglefjellet	H.U. Sverdrupfjella	−72.2900	0.7909	1930	AFT	AHe
Z7.24.3	Granite dyke	Fuglefjellet	H.U. Sverdrupfjella	−72.2910	0.7813	1850	AFT	
Z7.25.1	Metavolcanic migmatite	Roerkulten	H.U. Sverdrupfjella	−72.2979	0.4000	1595	AFT	AHe ZHe
Z7.25.3	Metavolcanic migmatite	Roerkulten	H.U. Sverdrupfjella	−72.2979	0.4000	1595	AFT	
Z7.1.4	Migmatite	Sofietoppen	Gjelsvikfjella	−72.0000	2.5167	1270	AFT	AHe
Z7.2.1	Migmatite	Risen	Gjelsvikfjella	−71.9719	3.3432	1825	AFT	AHe
Z7.41.1	Syenite	Stabben	Gjelsvikfjella	−71.9500	2.7833	1200	AFT	AHe
Z7.6.1	Migmatite	Vedkosten	Hochlinfjellet	−72.0425	3.9583	1900	AFT	
Z7.9.2	Monzonite/syenite	Stålstuten	Hochlinfjellet	−72.0477	4.1754	1780	AFT	AHe
Z7.10.1	Monzonite	Hoggestabben	Hochlinfjellet	−72.0054	3.9804	1765	AFT	AHe
Z7.11.2	Metased. gray migmatite	Vedskålen	Hochlinfjellet	−72.0412	3.9165	1915	AFT	
Z7.11.3	Grt-rich layer in layered migmatite	Vedskålen	Hochlinfjellet	−72.0412	3.9165	1915	AFT	
Z7.11.4	Amphibolite + Qtz-fsp layer	Vedskålen	Hochlinfjellet	−72.0412	3.9165	1915	AFT	AHe ZHe

zircon were concentrated using standard techniques, including crushing, Holman-Wilfley shaking table and magnetic and heavy-liquid separation techniques.

A wide temperature range is covered by combining apatite and zircon (U–Th)/He data with apatite fission track data. Whereas the AFT system has a partial annealing zone from c. 60–120 °C (Gleadow and Duddy, 1981), the partial retention zones of the AHe and ZHe systems have traditionally been assigned to 35–75 °C and 200–230 °C, respectively (Farley and Stockli, 2002; Reiners et al., 2002). However, more recent studies have proven that the closure temperatures of the (U–Th)/He systems are strongly affected by radiation damage (Shuster et al., 2006; Guenther et al., 2013).

4.1. Apatite fission track analyses

Thirty-four samples were analyzed by the apatite fission track (AFT) technique, using the external detector method (Gleadow, 1981). The apatite grains used for fission track analyses were mounted in epoxy and ground and polished to expose an internal crystal surface. The

apatite mounts were etched for 20 s in 5 M nitric acid at 20 ± 0.5 °C to reveal the spontaneous fission tracks. External mica detectors were placed on the AFT mounts, and the sample sandwiches were irradiated at the FRM II research reactor at the Technical University Munich (Germany), using a thermal neutron flux of 1 × 10¹⁶ neutrons/cm². The neutron flux was monitored by using the dosimeter glasses IRMM-540R. Finally, the external mica detectors were etched in 40% hydrofluoric acid at room temperature for 20 min to reveal the induced tracks.

The AFT analyses were conducted at the Department of Earth Science, University of Bergen, Norway, using an Olympus BX51 optical microscope equipped with a computer-driven stage and the FT-Stage software (Dumitru, 1993). A magnification of 1250× was used for fission track counting. The AFT ages were calculated by the TrackKey software (Dunkl, 2002), using the zeta calibration approach (Hurford and Green, 1983), with a zeta calibration factor of 214 ± 5 (H. Sirevaag) or 234 ± 3 (A. Ksienzyk).

Etch pit diameter (Dpar; Donelick et al., 2005) and confined track length measurements were conducted at a magnification of

Table 2
Apatite fission track data from western Dronning Maud Land.

Sample	Region	Elevation	Sample quality	Analyst	n (G)	Spontaneous		Induced		ρ_d	N_d	$P(\chi^2)$ (%)	Disp.	U (ppm)	Dpar (μm)	$\pm 1\sigma$ (μm)	Central age (Ma)	$\pm 1\sigma$ (Ma)	Measured		C-axis proj.		n (TL)	
						ρ_s	N_s	ρ_i	N_i										MTL (μm)	$\pm 1\sigma$ (μm)	MTL (μm)	$\pm 1\sigma$ (μm)		
Grunehogna Province																								
Z7.29.10	ADT	1878	P, d, i, s	HS	20	8.55	326	17.68	674	18.155	42255	34	0.16	14	1.28	0.10	95	8						
				AK	28	6.42	390	15.05	915	17.951	33531	90	0.00	12			89	6						
Z7.30.1	ADT	1670	F, d, i, s	HS	20	10.55	617	21.46	1255	18.075	42255	39	0.03	17	1.28	0.08	94	5	12.4	1.7	13.6	1.3	51	
				AK	30	9.20	766	20.87	1738	17.889	33531	30	0.02	15			91	4						
Z7.36.1	Ahl	1129	VP, d, i	HS	19	2.99	136	3.25	148	17.995	42255	44	0.15	3	1.45	0.22	175	22						
				AK	20	2.69	122	3.29	149	17.827	33531	88	0.00	3			168	21						
Z7.36.7	Ahl	974	VP, d, i, s	HS	20	4.09	130	3.80	121	17.915	42255	100	0.00	3	1.45	0.12	203	26						
				AK	21	3.39	111	3.85	126	17.766	33531	100	0.00	3			180	24						
GG99	Ahl	1394	G, i	HS	19	16.26	619	11.38	427	20.711	35707	85	0.00	8	1.80	0.11	309	21	11.9	1.9	13.1	1.5	100	
Maud Belt - West of EAAO																								
J7.2.94/4	HF	1300	G, (z/wz)	HS	20	30.35	1341	64.38	2845	20.376	35707	27	0.08	47	1.50	0.16	102	5	11.5	1.8	12.9	1.4	100	
BB1600	HF	1600	F	HS	20	21.20	751	42.56	1508	20.767	35707	0	0.25	31	1.35	0.14	111	9	11.8	1.6	13.1	1.2	100	
J8.2.94/6	HF	2100	G, z, (i)	HS	22	13.57	654	22.85	1101	20.320	35707	6	0.17	17	1.44	0.08	132	9	12.1	2.0	13.3	1.5	100	
ST7	HF	2100	F, (wz)	HS	22	38.34	1667	70.33	3058	19.146	35707	6	0.09	51	1.30	0.08	110	5	11.8	1.5	13.1	1.1	100	
93/75	KV	2000	G/F, i, z/wz	HS	25	70.13	3702	51.43	2714	20.823	35707	0	0.17	36	1.35	0.09	302	15	11.4	1.6	12.9	1.1	100	
93/57	KV	2250	F, (z/wz)	HS	20	71.98	2558	53.83	1913	20.879	35707	13	0.09	38	1.45	0.11	292	13	12.3	1.4	13.5	1.0	100	
MDB51A	MBR	1530	VG	HS	20	39.26	1335	37.35	1270	17.745	39603	55	0.03	31	1.49	0.11	197	9	12.6	1.9	13.8	1.4	100	
Z7.26.1	HUS	1272	G	HS	20	9.27	771	19.49	1621	19.018	41977	76	0.01	15	1.32	0.12	96	5	12.8	1.5	13.9	1.2	65	
Z7.26.6	HUS	1246	VP, d, i	HS	20	6.07	420	10.59	733	18.235	42255	12	0.19	8	1.24	0.11	115	9						
				AK	28	5.23	451	10.19	879	18.012	33531	0	0.34	8			115	11						
Z7.27.6	HUS	929	F, d, wz	HS	20	10.20	692	20.21	1371	17.992	39603	9	0.10	16	1.42	0.10	98	6	13.2	1.4	14.2	1.1	81	
Maud Belt - EAAO																								
92/10	KV	2100	P, s, z/wz	HS	20	56.27	1898	46.04	1553	17.696	39603	39	0.06	37	1.51	0.10	229	10	12.0	2.1	13.3	1.5	100	
H-10	HUS	1000	F (d, z)	HS	22	18.32	895	38.90	1900	17.647	39603	2	0.15	33	1.39	0.12	89	5	13.0	1.7	14.1	1.3	100	
Z7.16.1	HUS	1435	G, s	HS	20	14.20	971	26.29	1798	18.484	39603	91	0.00	22	1.40	0.13	106	5	12.7	1.6	13.9	1.2	100	
Z7.18.5	HUS	1474	G, s	HS	20	17.12	1811	34.61	3662	18.314	42255	42	0.03	27	1.28	0.09	96	4	13.3	1.2	14.3	1.0	100	
				AK	25	12.51	1685	28.41	3827	18.074	33531	54	0.00	22			92	3						
Z7.19.1	HUS	1508	G	HS	20	7.57	712	13.06	1228	18.394	42255	17	0.09	10	1.49	0.13	114	7	13.5	1.6	14.4	1.2	52	
				AK	30	7.09	944	13.94	1856	18.136	33531	82	0.00	11			107	5						
Z7.22.2	HUS	1785	F, z	HS	21	37.94	1959	52.58	2715	18.435	39603	0	0.12	36	1.38	0.12	139	7	13.2	1.8	14.3	1.2	93	
Z7.24.2	HUS	1932	P, (d)	HS	20	5.60	396	9.50	672	18.386	39603	33	0.08	8	1.40	0.09	115	8	12.9	1.8	13.8	1.5	50	
Z7.24.3	HUS	1848	F, (d, s)	HS	20	18.76	1249	40.01	2664	18.287	39603	99	0.00	31	1.24	0.13	91	4	13.2	1.7	14.2	1.3	86	
Z7.25.1	HUS	1595	G, z/wz	HS	22	22.43	1858	44.95	3724	18.238	39603	7	0.05	38	1.35	0.12	97	4	12.8	1.8	14.0	1.2	100	
Z7.25.3	HUS	1595	G, z	HS	22	18.41	1246	32.80	2220	18.041	39603	11	0.04	27	1.41	0.11	108	5	13.2	1.5	14.1	1.1	100	
Z7.1.4	GjF	1270	F, s, (i)	HS	20	9.62	656	18.83	1284	18.879	39603	54	0.01	15	1.29	0.09	102	6	12.7	1.9	13.6	1.6	72	
Z7.2.1	GjF	1823	F, s, z/wz	HS	20	14.83	851	20.09	1153	18.829	39603	64	0.01	17	1.18	0.10	147	8	13.1	1.8	14.1	1.4	100	
Z7.41.1	GjF	1200	F, s	HS	20	22.75	1084	30.69	1462	17.942	39603	83	0.00	25	1.27	0.08	141	7	12.9	1.7	14.0	1.3	100	
Z7.6.1	HoF	1900	F, d, s, z/wz	HS	20	48.83	2377	46.42	2260	18.780	39603	6	0.09	37	1.25	0.14	210	9	12.1	1.9	13.4	1.4	100	
Z7.9.2	HoF	1780	G, s	HS	19	15.62	744	13.60	648	18.731	39603	0	0.25	12	1.36	0.14	229	19	12.5	2.1	13.5	1.6	46	
Z7.10.1	HoF	1765	P, s, z/wz	HS	20	36.79	1406	33.02	1262	18.682	39603	28	0.08	26	1.30	0.07	219	11	12.0	1.9	13.3	1.5	100	
Z7.11.2	HoF	1915	F, s	HS	20	24.04	1718	17.70	1267	18.632	39603	15	0.11	13	1.33	0.09	265	14	11.7	1.9	13.0	1.4	100	
Z7.11.3	HoF	1915	F, (s)	HS	21	83.28	4866	64.20	3751	18.583	39603	70	0.01	52	1.66	0.12	253	8	12.2	1.6	13.5	1.0	99	
Z7.11.4	HoF	1915	F, s	HS	20	59.77	2808	53.66	2521	18.534	39603	13	0.07	45	1.32	0.13	218	9	11.8	2.0	13.2	1.5	100	

n(G): number of dated grains; n(TL): number of measured track lengths; $N_{s,i,d}$: number of spontaneous (N_s) and induced (N_i) tracks and number of tracks counted on dosimeter glass IRMM-540R (N_d); $\rho_{s,i,d}$: track densities (1×10^5 tracks cm^{-2}); $P(\chi^2)$: p -value of the chi-square homogeneity test (Galbraith, 2005); Disp: dispersion; Dpar: etch pit diameter; MTL: mean track length.

Regions: ADT: Annandagstoppane; Ahl: Ahlmannryggen; GjF: Gjelsvikfjella; HF: Heimefrontfjella; HoF: Hochlinfjellet; HUS: H.U. Sverdrupfjella; KV: Kirwanveggen; MBR: Midbresrabben.

Sample quality: VG: very good; G: good; F: fair; P: poor; VP: very poor; d: dislocations; i: inclusions; s: scratches; z/wz: zoned/weakly zoned. Letters in brackets correspond to grain features that only affect few grains in the sample.

Samples in black are counted by H. Sirevaag ($\zeta_{\text{IRMM-540R}}=214 \pm 5$). Italic samples are replicate analyses, counted by A. Ksienzyk ($\zeta_{\text{IRMM-540R}}=234 \pm 3$).

Table 3

Apatite (ap) and zircon (zr) (U–Th)/He analyses. Excluded analyses (see text for explanation) are marked in *italic* and the reason for exclusion is given to the right of the table.

Sample	Mineral	# Term.	Sphere radius [μm]	He		²³⁸ U		²³² Th		Sm		eU		Ejection correction [Ft]	Uncorr. He-age [Ma]	Ft-Corr. He-age [Ma]	Unweighted sample average [Ma]		Reason					
				Vol. [ncc]	1σ [%]	Mass [ng]	1σ [%]	Conc. [ppm]	Mass [ng]	1σ [%]	Conc. [ppm]	Th/U ratio	Mass [ng]				1σ [%]	Conc. [ppm]		Age	±1σ			
Grunehogna Province																								
Z7.29.10 a1	Ap	1	44	0.148	3.5	0.009	6.6	6.2	0.011	3.3	7.4	1.20	0.595	9.1	409	8	0.64	74	116	9	8	109	35	Re-extract
Z7.29.10 a2	Ap	2	50	0.549	2.4	0.027	2.8	9.5	0.020	2.9	7.0	0.74	1.201	9.1	428	11	0.68	109	161	10	6			
Z7.29.10 a3	Ap	2	45	0.535	2.3	0.043	2.3	16.6	0.035	2.6	13.4	0.81	1.449	9.1	559	20	0.64	70	108	7	6			
Z7.29.10 a4	Ap	2	43	0.193	3.5	0.014	4.5	7.4	0.016	3.0	8.6	1.16	0.789	3.0	425	9	0.63	66	106	8	7			
Z7.29.10 a5	Ap	2	40	0.193	2.4	0.038	2.6	12.6	0.004	4.8	1.3	0.11	0.436	8.1	146	13	0.61	38	62	4	7			
Z7.30.1 a1	Ap	1	57	0.586	1.6	0.043	2.2	17.3	0.028	2.8	11.4	0.66	1.382	3.4	552	20	0.73	79	108	5	5	105	16	
Z7.30.1 a2	Ap	1	66	0.921	1.5	0.093	1.9	25.4	0.059	2.6	15.9	0.63	2.133	3.4	579	29	0.76	61	80	3	4			
Z7.30.1 a3	Ap	0	58	0.603	1.6	0.050	2.1	17.6	0.049	2.6	17.6	1.00	1.175	3.5	417	22	0.74	70	95	4	5			
Z7.30.1 a4	Ap	1	73	2.115	1.6	0.139	1.9	20.9	0.108	2.5	16.2	0.77	3.077	4.8	463	25	0.81	92	114	4	4			
Z7.30.1 a5	Ap	1	48	0.835	1.7	0.053	2.1	17.5	0.042	2.6	13.6	0.78	2.050	7.1	673	21	0.68	86	127	7	6			
Z7.36.1 a1	Ap	0	60	0.211	3.3	0.015	4.4	2.5	0.064	2.5	10.9	4.39	1.813	9.1	306	5	0.73	39	53	3	6	50	3	
Z7.36.1 a2	Ap	0	72	0.169	3.7	0.010	5.9	2.2	0.078	2.5	16.8	7.73	1.373	9.1	294	6	0.77	35	45	3	6			
Z7.36.1 a3	Ap	0	60	0.096	4.8	0.006	11.0	1.8	0.036	2.6	12.0	6.58	0.836	9.1	278	5	0.73	38	52	4	8			
Z7.38.3 a1	Ap	2	32	0.103	2.2	0.012	5.2	15.5	0.015	3.2	19.4	1.25	0.046	5.1	59	20	0.50	53	106	9	9	100	9	
Z7.38.3 a2	Ap	2	36	0.069	2.6	0.004	16.7	3.5	0.017	3.1	15.4	4.43	0.247	4.0	221	7	0.53	57	107	11	10			
Z7.38.3 a3	Ap	2	45	0.965	0.9	0.118	1.9	90.3	0.062	2.5	47.6	0.53	0.579	4.4	441	101	0.66	58	87	5	5			
GG99 a1	Ap	0	98	1.629	1.7	0.077	2.0	9.8	0.293	2.4	37.1	3.79	3.639	7.0	461	19	0.84	76	90	3	3	85	7	
GG99 a2	Ap	0	64	0.852	1.7	0.042	2.3	8.2	0.171	2.4	33.5	4.11	2.381	7.0	467	16	0.76	69	91	4	4			
GG99 a3	Ap	0	74	0.412	1.8	0.024	3.0	8.5	0.092	2.5	32.3	3.79	1.345	7.1	473	16	0.80	60	75	3	4			
Maud Belt - West of EAAO																								
J7.2.94/4 a2	Ap	0	57	0.877	1.4	0.083	1.9	40.5	0.149	2.5	72.9	1.80	0.584	3.5	285	58	0.72	59	81	4	5	90	16	
J7.2.94/4 a3	Ap	0	54	0.135	2.1	0.014	4.6	15.3	0.022	3.0	23.5	1.53	0.107	4.4	117	21	0.71	55	78	4	6			
J7.2.94/4 a4	Ap	2	51	4.900	1.6	0.329	1.8	86.1	0.781	2.4	204.7	2.38	1.744	4.7	457	134	0.68	76	113	6	5			
BB1600 a1	Ap	1	46	0.365	1.7	0.046	2.2	24.8	0.005	4.0	2.6	0.10	0.823	3.5	444	25	0.67	56	83	5	6	89	13	
BB1600 a2	Ap	1	46	0.996	1.5	0.101	1.9	50.7	0.006	3.9	3.2	0.06	0.849	3.4	425	51	0.68	75	111	6	5			
BB1600 a3	Ap	1	60	0.564	1.6	0.075	2.0	21.1	0.003	4.4	0.9	0.04	1.261	3.5	353	21	0.75	54	72	3	4			
BB1600 a4	Ap	2	34	0.148	2.1	0.025	3.0	25.7	0.000	-461.5	0.0	0.00	0.266	8.0	277	26	0.54	46	85	7	8			
BB1600 a5	Ap	1	37	0.246	2.0	0.031	2.6	15.7	0.003	4.7	1.5	0.09	0.638	7.3	327	16	0.59	56	95	7	7			
J8.2.94/6 a1	Ap	2	55	0.499	1.6	0.056	2.1	8.7	0.021	2.9	3.2	0.37	2.133	3.4	329	9	0.72	52	72	3	5	74	6	
J8.2.94/6 a2	Ap	0	65	0.211	1.8	0.025	2.9	9.8	0.015	3.2	5.9	0.61	0.662	3.6	261	11	0.77	52	67	3	4			
J8.2.94/6 a3	Ap	2	50	0.399	1.7	0.042	2.2	16.8	0.036	2.7	14.3	0.85	0.940	3.5	373	20	0.68	56	82	4	5			
ST7 a1	Ap	2	66	0.893	1.4	0.146	1.9	23.8	0.017	3.1	2.8	0.12	0.828	3.5	135	24	0.76	47	62	3	4	72	9	
ST7 a2	Ap	1	50	0.527	1.5	0.059	2.1	34.6	0.047	2.6	27.1	0.78	0.559	3.7	326	41	0.69	58	84	4	5			
ST7 a3	Ap	0	94	0.986	1.4	0.119	1.9	26.3	0.025	2.9	5.6	0.21	0.933	3.4	207	28	0.86	61	71	2	3			
93/57 a1	Ap	1	37	2.412	1.7	0.057	2.1	169.1	0.111	2.5	330.0	1.95	0.039	10.4	116	247	0.57	235	413	28	7	406	52	
93/57 a2	Ap	1	48	2.256	1.7	0.047	2.3	70.5	0.144	2.5	217.7	3.09	0.055	10.4	83	122	0.66	226	344	19	6			
93/57 a3	Ap	2	46	3.394	1.7	0.070	2.0	32.4	0.214	2.4	99.7	3.08	0.180	8.4	84	56	0.64	227	353	20	6			
93/57 a4	Ap	2	39	3.976	1.1	0.078	2.0	18.9	0.192	2.5	46.4	2.46	0.168	7.0	41	30	0.58	259	445	29	7			
93/57 a5	Ap	1	43	3.314	1.1	0.071	2.1	18.1	0.063	34.2	16.2	0.90	0.210	7.9	54	22	0.64	307	477	39	8			
MDB50 a1	Ap	2	57	3.034	1.1	0.179	1.9	28.3	0.308	2.4	48.6	1.72	0.510	7.3	81	40	0.72	97	136	6	5	138	18	
MDB50 a2	Ap	2	40	1.431	1.1	0.085	2.0	21.2	0.132	2.5	32.7	1.54	0.189	8.3	47	29	0.60	100	166	11	6			
MDB50 a3	Ap	1	46	0.823	1.2	0.068	2.1	15.5	0.068	2.6	15.4	0.99	0.112	8.2	25	19	0.66	79	120	7	5			
MDB50 a4	Ap	1	52	1.780	1.1	0.123	1.9	21.1	0.161	2.5	27.7	1.32	0.200	7.5	34	28	0.71	90	128	6	5			
MDB51A a1	Ap	2	48	0.917	1.5	0.060	2.0	26.2	0.114	2.5	49.9	1.91	0.271	4.0	119	38	0.66	85	129	7	6	147	11	
MDB51A a2	Ap	2	38	0.443	1.7	0.030	2.6	33.4	0.056	2.6	63.7	1.91	0.111	4.4	126	48	0.56	83	148	10	7			
MDB51A a3	Ap	2	52	1.446	1.5	0.079	2.0	30.3	0.106	2.5	40.6	1.34	0.282	3.8	108	40	0.71	112	157	8	5			
MDB51A a4	Ap	2	44	1.366	1.5	0.077	2.0	29.1	0.164	2.5	62.4	2.14	0.267	4.0	101	44	0.62	95	154	9	6			
Z7.26.1 a1	Ap	0	61	0.507	2.4	0.029	2.7	5.0	0.245	2.4	42.3	8.46	2.937	9.0	506	15	0.73	38	51	3	5	50	4	
Z7.26.1 a2	Ap	1	64	0.561	2.4	0.020	3.3	4.5	0.423	2.4	94.3	20.85	2.102	9.1	468	27	0.74	34	45	2	5			
Z7.26.1 a3	Ap	0	67	0.796	2.1	0.035	2.5	4.8	0.402	2.4	56.2	11.62	3.626	9.0	506	18	0.75	41	54	3	5			
Z7.27.6 a1	Ap	2	41	0.029	3.9	0.004	17.4	2.2	0.000	-133.9	0.0	0.00	0.107	4.4	64	2	0.62	54	86	13	15	68	10	

Z7.27.6 a2	Ap	1	52	0.077	2.5	0.013	4.7	4.2	0.001	25.9	0.3	0.08	0.040	4.8	13	4	0.70	48	68	5	7		
Z7.27.6 a3	Ap	2	43	0.027	3.8	0.006	10.8	2.6	0.003	4.4	1.5	0.56	0.023	8.2	11	3	0.64	35	55	6	11		
Z7.27.6 a4	Ap	0	69	0.030	3.4	0.005	12.3	2.2	0.001	16.8	0.6	0.26	0.016	7.9	8	2	0.80	47	59	7	12		
Z7.27.6 a5	Ap	2	50	0.204	2.0	0.035	2.4	11.6	0.002	5.7	0.8	0.07	0.110	5.8	37	12	0.68	46	68	4	6		
Z7.27.6 a6	Ap	2	42	0.015	4.2	0.002	26.8	1.2	0.001	15.7	0.7	0.56	0.015	10.7	8	1	0.63	47	75	17	23		
J8.2.94/6 z1	Zr	2	51	66.146	0.7	1.499	1.8	367.2	0.369	2.4	90.3	0.25	0.006	22.9	1	388	0.76	335	441	18	4	448	5
J8.2.94/6 z2	Zr	2	53	84.253	0.7	1.799	1.8	259.0	0.649	2.4	93.4	0.36	0.022	10.4	3	281	0.77	347	451	18	4		
J8.2.94/6 z3	Zr	2	51	44.781	0.7	0.974	1.8	246.6	0.325	2.4	82.2	0.33	0.003	33.9	1	266	0.76	342	452	18	4		
K1-1 z1	Zr	2	30	6.481	0.7	0.282	1.9	304.4	0.029	3.0	31.0	0.10	0.001	51.0	1	312	0.62	183	297	18	6	294	65
K1-1 z2	Zr	2	30	11.539	0.7	0.509	1.8	557.8	0.106	2.5	116.1	0.21	0.000	100.1	0	585	0.62	176	287	17	6		
K1-1 z4	Zr	2	40	17.630	1.6	0.504	1.8	153.0	0.077	2.5	23.0	0.15	0.021	12.4	6	158	0.70	273	388	20	5		
K1-1 z5	Zr	2	38	10.990	1.6	0.620	1.8	208.0	0.092	2.4	31.0	0.15	0.089	7.9	30	216	0.69	140	204	11	5		
KV-1 z1	Zr	2	50	54.658	1.6	0.881	1.8	205.4	0.424	2.4	98.9	0.48	0.068	8.1	16	229	0.75	444	590	26	4	579	64
KV-1 z2	Zr	2	46	17.952	1.6	0.256	1.9	88.0	0.177	2.4	61.0	0.69	0.166	8.0	57	102	0.73	478	651	30	5		
KV-1 z3	Zr	2	39	18.385	1.6	0.390	1.8	201.5	0.173	2.4	89.3	0.44	0.049	9.1	25	223	0.69	343	495	26	5		
93/57 z1	Zr	2	54	61.210	1.6	1.103	1.8	182.0	1.123	2.4	185.0	1.02	0.173	7.9	29	225	0.77	359	468	19	4	466	59
93/57 z2	Zr	2	53	71.360	1.6	1.446	1.8	228.0	1.090	2.4	172.0	0.75	0.271	7.8	43	268	0.77	337	439	18	4		
93/57 z3	Zr	2	57	103.890	1.6	1.598	1.8	196.0	1.270	2.4	156.0	0.79	0.216	7.5	26	232	0.78	437	558	22	4		
93/57 z5	Zr	2	45	32.400	1.1	0.791	1.8	191.2	0.469	2.4	113.3	0.59	0.068	5.5	16	218	0.73	290	398	18	4		
MDB50 z1	Zr	2	73	82.300	1.0	1.725	1.8	127.7	1.056	2.4	78.2	0.61	0.045	5.8	3	146	0.83	335	406	13	3	405	9
MDB50 z2	Zr	2	60	44.200	1.0	0.995	1.8	121.6	0.615	2.4	75.1	0.62	0.022	9.2	3	139	0.79	313	394	14	4		
MDB50 z3	Zr	2	53	40.600	1.1	0.883	1.8	122.0	0.613	2.4	84.7	0.69	0.035	6.4	5	142	0.77	318	415	16	4		

Maud Belt - EAAO

92/10 a1	Ap	1	61	2.976	1.4	0.083	1.9	28.3	0.021	2.9	7.2	0.26	0.469	3.7	159	30	0.75	261	350	15	4	315	37
92/10 a2	Ap	1	60	4.875	1.4	0.195	1.8	64.3	0.034	2.7	11.3	0.18	0.960	3.4	317	67	0.75	188	252	11	4		
92/10 a3	Ap	1	55	2.854	1.4	0.091	1.9	42.0	0.040	2.7	18.2	0.43	0.458	3.6	210	46	0.71	222	311	15	5		
92/10 a4	Ap	2	45	1.517	1.7	0.050	2.1	32.6	0.008	3.8	5.5	0.17	0.180	8.3	118	34	0.65	232	356	21	6		
92/10 a5	Ap	1	54	1.931	1.7	0.066	2.0	23.8	0.004	4.1	1.6	0.07	0.358	7.5	129	24	0.73	224	309	6	2		
SIS33 a1	Ap	2	52	0.319	2.6	0.008	7.3	2.8	0.040	2.6	13.9	4.94	1.858	10.1	641	6	0.68	80	117	9	7	95	16
SIS33 a2	Ap	2	33	0.083	4.6	0.003	18.0	3.7	0.017	10.0	21.6	5.79	0.860	2.8	1066	9	0.49	37	76	9	11		
SIS33 a3	Ap	2	40	0.240	3.0	0.007	9.1	2.9	0.039	2.6	16.9	5.86	1.870	10.2	810	7	0.59	63	107	9	9		
SIS33 a4	Ap	0	47	0.135	4.4	0.003	20.3	1.8	0.018	2.9	10.3	5.59	1.233	2.9	715	4	0.66	64	96	8	8		
SIS33 a6	Ap	0	64	0.225	1.9	0.007	7.8	2.4	0.034	2.7	11.1	4.52	2.012	4.8	658	5	0.75	58	77	4	5		
H-10 a1	Ap	1	45	0.920	1.5	0.089	1.9	54.0	0.004	4.0	2.5	0.05	0.187	4.4	113	55	0.66	82	125	7	6	110	39
H-10 a2	Ap	0	57	0.033	3.6	0.005	11.6	2.4	0.000	-236.0	0.0	0.00	0.064	5.0	31	2	0.74	48	65	7	11		
H-10 a3	Ap	2	39	0.174	2.0	0.017	3.6	8.1	0.001	20.3	0.5	0.06	0.105	4.4	49	8	0.60	77	129	9	7		
H-10 a4	Ap	2	49	1.376	1.5	0.095	1.9	32.9	0.005	3.9	1.9	0.06	0.358	3.7	124	33	0.68	114	166	9	5		
H-10 a6	Ap	2	57	0.141	2.1	0.023	3.1	5.1	0.000	124.6	0.1	0.02	0.099	8.9	22	5	0.73	49	67	4	5		
Z7.16.1 a1	Ap	2	64	2.866	0.8	0.125	1.9	25.3	0.679	2.4	137.5	5.44	1.218	4.3	247	58	0.74	80	108	5	4	101	5
Z7.16.1 a2	Ap	2	103	9.846	0.7	0.386	1.8	20.7	2.469	2.4	132.6	6.40	5.331	4.2	286	52	0.83	80	96	3	3		
Z7.16.1 a3	Ap	1	89	9.169	0.7	0.385	1.8	29.7	2.150	2.4	165.6	5.58	4.549	4.2	350	69	0.81	81	99	3	3		
Z7.19.1 a1	Ap	2	50	0.120	4.2	0.014	4.6	4.5	0.000	-132.2	0.0	0.00	0.035	10.8	12	5	0.73	70	96	7	7	93	10
Z7.19.1 a2	Ap	2	58	0.236	3.0	0.026	2.8	4.6	0.000	-47.1	0.0	0.00	0.054	10.2	10	5	0.74	72	97	5	6		
Z7.19.1 a3	Ap	2	68	0.114	3.8	0.011	5.4	1.8	0.000	202.0	0.0	0.01	0.579	9.1	94	2	0.77	59	76	5	7		
Z7.19.1 a4	Ap	2	45	0.069	5.7	0.009	10.0	3.6	0.004	6.0	1.8	0.51	0.025	7.4	11	4	0.66	26	40	5	12		Error
Z7.19.1 a5	Ap	2	51	0.378	1.9	0.042	2.4	10.4	0.002	6.5	0.4	0.04	0.054	9.3	13	10	0.72	72	101	5	5		
Z7.22.2 a1	Ap	2	52	1.417	1.4	0.111	1.9	41.8	0.016	3.2	5.9	0.14	0.144	4.8	54	43	0.71	100	141	7	5	142	26
Z7.22.2 a2	Ap	2	58	0.738	1.5	0.065	2.0	22.9	0.007	3.8	2.5	0.11	0.107	5.2	38	23	0.73	90	123	6	5		
Z7.22.2 a3	Ap	1	65	5.223	1.3	0.291	1.8	58.5	0.045	2.6	9.0	0.15	0.295	3.8	59	61	0.76	141	184	8	4		
Z7.22.2 a4	Ap	2	64	1.083	1.7	0.080	1.9	26.7	0.080	2.5	26.8	1.00	0.158	5.5	53	33	0.75	89	118	5	4		
Z7.22.2 a5	Ap	1	44	1.120	1.7	0.044	2.2	16.5	0.005	4.0	1.8	0.11	0.105	5.8	40	17	0.65	200	308	18	6		Outlier
Z7.24.2 a1	Ap	2	45	0.188	1.6	0.019	4.2	4.5	0.021	3.1	4.9	1.08	0.294	8.1	68	6	0.65	58	90	6	6	92	2
Z7.24.2 a2	Ap	2	46	0.157	1.7	0.015	5.5	3.1	0.012	3.5	2.3	0.75	0.330	6.8	66	4	0.65	62	95	6	7		
Z7.24.2 a3	Ap	2	57	3.558	1.0	0.047	2.5	6.8	0.051	2.7	7.3	1.08	0.791	7.3	113	9	0.72	432	598	28	5		Outlier
Z7.25.1 a3	Ap	1	53	0.340	1.7	0.042	2.3	23.5	0.032	2.7	17.8	0.76	0.095	5.9	53	28	0.71	55	78	4	5	132	34
Z7.25.1 a4	Ap	2	51	0.661	1.7	0.043	2.2	15.9	0.012	3.3	4.4	0.28	0.081	6.2	30	17	0.69	117	170	9	5		
Z7.25.1 a5	Ap	2	43	0.406	1.8	0.038	2.3	20.2	0.007	3.7	3.6	0.18	0.064	5.9	34	21	0.64	83	131	8	6		
Z7.25.1 a7	Ap	2	38	0.165	1.6	0.019	4.3	5.5	0.003	13.0	1.0	0.17	0.036	8.4	10	6	0.58	66	113	9	8		
Z7.25.1 a8	Ap	2	49	0.510	1.3	0.047	2.5	7.9	0.011	3.2	1.8	0.24	0.083	7.2	14	8	0.69	83	122	7	5		
Z7.25.1 a9	Ap	2	41	0.858	1.2	0.059	2.2	12.6	0.014	3.3	3.1	0.24	0.109	8.4	23	13	0.62	111	178	11	6		
Z7.1.4 a1	Ap	2	44	0.304	1.4	0.021	3.5	12.2	0.008	3.5	4.9	0.40	0.924	3.7	532	13	0.66	81	124	7	6	122	8
Z7.1.4 a2	Ap	2	54	0.960	1.1	0.066	2.0	23.1	0.034	2.7	11.9	0.51	1.356	3.3	473	26	0.71	92					

Table 3 (continued)

Sample	Mineral	# Term.	Sphere radius [μm]	He		²³⁸ U		²³² Th		Sm				Ejection correction [Ft]		Uncorr. He-age [Ma]	Ft-Corr. He-age [Ma]	1σ [Ma]	1σ [%]	Unweighted sample average [Ma]		Reason		
				Vol. [ncc]	1σ [%]	Mass [ng]	1σ [%]	Conc. [ppm]	Mass [ng]	1σ [%]	Conc. [ppm]	Th/U ratio	Mass [ng]	1σ [%]	Conc. [ppm]					eU [ppm]	Age		±1σ	
Z7.1.4 a3	Ap	2	36	0.384	2.8	0.007	8.5	11.2	0.012	3.4	18.9	1.69	0.308	3.7	481	16	0.55	249	449	39	9		Outlier	
Z7.1.4 a4	Ap	2	51	0.280	1.4	0.014	4.6	5.5	0.015	3.1	5.8	1.06	1.438	3.4	555	7	0.70	78	111	6	5			
Z7.2.1 a1	Ap	2	37	0.033	3.2	0.003	24.0	4.2	0.004	4.5	5.9	1.40	0.121	3.9	181	6	0.57	57	101	16	16	159	29	Error "Too old"; inclusion
Z7.2.1 a2	Ap	2	41	1.042	1.2	0.044	2.3	32.0	0.006	3.8	4.4	0.14	0.953	3.4	686	33	0.63	159	252	15	6			
Z7.2.1 a3	Ap	2	38	0.135	1.9	0.005	14.1	4.7	0.005	4.1	4.9	1.03	0.455	4.2	425	6	0.59	110	188	18	10			
Z7.2.1 a4	Ap	2	50	0.270	1.4	0.022	3.1	11.3	0.003	4.4	1.7	0.15	0.269	4.7	139	12	0.69	90	131	7	6			
Z7.41.1 a1	Ap	2	58	2.196	1.4	0.089	1.9	22.3	0.320	2.4	79.7	3.58	2.288	3.4	570	41	0.74	98	132	6	4	109	15	
Z7.41.1 a3	Ap	1	45	0.400	1.7	0.022	3.2	19.1	0.119	2.5	105.1	5.52	0.928	3.5	818	44	0.63	57	91	6	6			
Z7.41.1 a4	Ap	1	40	0.604	1.7	0.021	3.1	16.9	0.207	2.4	166.2	9.82	0.929	4.8	745	56	0.58	64	110	7	7			
Z7.41.1 a5	Ap	1	52	0.624	1.7	0.020	3.3	6.9	0.178	2.4	62.3	9.03	1.560	4.8	547	22	0.67	69	103	6	6			
Z7.9.2 a2	Ap	1	49	0.640	1.0	0.030	2.8	24.6	0.078	2.5	64.4	2.62	1.015	4.6	842	40	0.66	93	141	8	5	138	3	
Z7.9.2 a3	Ap	1	44	0.648	1.0	0.034	2.5	14.4	0.081	2.5	34.9	2.42	1.143	4.4	492	23	0.64	86	135	8	6			
Z7.10.1 a1	Ap	1	50	3.904	1.3	0.144	1.9	61.3	0.120	2.5	51.4	0.84	1.013	3.4	432	73	0.69	177	256	13	5	229	20	
Z7.10.1 a2	Ap	1	47	0.787	1.4	0.035	2.4	20.9	0.035	2.7	21.2	1.01	0.376	3.8	226	26	0.66	139	210	12	6			
Z7.10.1 a3	Ap	1	53	4.541	1.3	0.177	1.8	61.0	0.190	2.4	65.6	1.08	2.092	3.4	721	76	0.70	155	221	11	5			
Z7.11.4 a1	Ap	0	41	0.203	2.0	0.017	3.7	31.2	0.002	5.7	4.2	0.13	0.176	4.3	314	32	0.63	86	135	9	7	161	40	
Z7.11.4 a2	Ap	1	40	2.538	1.4	0.144	1.9	139.2	0.116	2.5	112.4	0.81	0.625	3.6	605	166	0.61	118	193	12	6			
Z7.11.4 a3	Ap	1	43	1.044	1.5	0.053	2.1	45.7	0.014	3.2	12.4	0.27	0.393	3.7	341	49	0.64	144	225	13	6			
Z7.11.4 a4	Ap	2	31	0.075	2.5	0.009	6.3	18.2	0.000	-213.7	0.0	0.00	0.137	5.9	269	18	0.49	60	122	12	10			
Z7.11.4 a5	Ap	1	35	0.146	2.1	0.014	4.2	23.3	0.001	15.7	2.0	0.09	0.180	5.3	291	24	0.57	74	131	10	8			
S1-24 z1	Zr	2	51	27.001	0.7	0.597	1.8	117.0	0.161	2.4	31.5	0.27	0.003	39.4	0	124	0.76	342	450	18	4	513	77	
S1-24 z2	Zr	2	55	24.030	0.7	0.570	1.8	105.0	0.095	2.6	17.5	0.17	0.006	18.5	1	109	0.78	326	420	16	4			
S1-24 z3	Zr	2	60	64.325	0.7	1.242	1.8	155.8	0.298	2.4	37.4	0.24	0.004	19.9	0	165	0.80	392	493	18	4			
S1-24 z4	Zr	2	53	21.146	1.6	0.361	1.8	64.4	0.077	2.5	13.7	0.21	0.027	11.3	5	68	0.77	444	579	24	4			
S1-24 z5	Zr	2	57	49.401	1.6	0.740	1.8	102.7	0.248	2.4	34.4	0.33	0.052	9.5	7	111	0.78	491	625	25	4			
H-10 z1	Zr	2	57	36.121	0.7	1.068	1.8	135.7	0.705	2.4	89.5	0.66	0.003	31.3	0	157	0.78	238	303	11	4	290	9	
H-10 z2	Zr	2	56	41.622	0.7	1.386	1.8	209.6	0.635	2.4	96.1	0.46	0.002	34.3	0	232	0.78	220	282	10	4			
H-10 z3	Zr	2	48	14.942	0.7	0.494	1.8	146.1	0.330	2.4	97.5	0.67	0.007	17.7	2	169	0.74	213	286	12	4			
Z7.25.1 z1	Zr	2	65	58.213	0.7	1.925	1.8	142.6	0.241	2.4	17.8	0.13	0.010	20.2	1	147	0.81	238	294	10	3	302	78	
Z7.25.1 z2	Zr	2	65	90.678	0.7	2.447	1.8	247.7	0.765	2.4	77.5	0.31	0.004	22.8	0	266	0.81	279	345	12	3			
Z7.25.1 z3	Zr	2	62	61.715	0.7	2.996	1.8	399.4	0.541	2.4	72.1	0.18	0.037	8.2	5	416	0.80	161	202	7	4			
Z7.25.1 z4	Zr	2	47	14.411	1.6	0.321	1.9	113.8	0.206	2.4	73.0	0.64	0.020	11.7	7	131	0.74	314	424	19	4			
Z7.25.1 z5	Zr	2	50	33.442	1.6	1.417	1.8	239.0	0.235	2.4	39.6	0.17	0.016	11.5	3	248	0.76	185	244	11	4			
Z7.11.4 z2	Zr	2	39	75.241	1.6	2.566	1.8	1344.0	1.113	2.4	583.0	0.43	0.029	10.6	15	1481	0.69	216	312	16	5	291	22	
Z7.11.4 z3	Zr	2	35	53.230	1.6	1.979	1.8	758.4	2.025	2.4	776.0	1.02	0.119	8.1	45	941	0.66	177	269	15	6			

Amount of helium is given in nano-cubic-cm in standard temperature and pressure.

Amount of radioactive elements are given in nanograms.

Ejection correct. (Ft): correction factor for alpha-ejection (according to Farley et al., 1996 and Hourigan et al., 2005).

Uncertainties of helium and the radioactive element contents are given as 1 sigma, in relative error %.

Uncertainties of the radioactive element concentrations are ca. 10% (due to the high uncertainty in the crystal mass estimation).

Uncertainty of the single grain age is given as 1 sigma in % and in Ma and it includes both the analytical uncertainty and the estimated uncertainty of the Ft.

Uncertainty of the sample average age is 1 standard deviation.

2000×. Dpar can be used as a proxy for apatite annealing kinetics, and at least five Dpars were measured for each grain that was counted, while at least three Dpars were measured for each track length. For the track lengths, only track-in-tracks (TinTs) were considered, and, where possible, 100 TinTs were measured for each sample.

4.2. (U–Th)/He analyses

Apatite grains from 31 samples and zircon grains from nine samples were dated by the (U–Th)/He method at the GÖchron Laboratories, Geoscience Center, University of Göttingen, Germany. Each sample was carefully evaluated: the grains were handpicked under binocular and petrographic microscopes to avoid fractures and mineral- and fluid-inclusions as far as possible. The selected crystals were photographed for determining grain dimensions before they were packed individually in platinum capsules. The ⁴He content was determined by degassing of the platinum capsules containing the crystals under high vacuum by heating with an infrared diode laser for 2 min. The extracted gas was purified with a SAES Ti–Zr getter at 450 °C and analyzed with a Hiden triple-filter quadrupole mass spectrometer, equipped with a positive ion-counting detector. The crystals were checked for complete degassing of He by sequential reheating and He measurement (re-extract).

In order to analyze the U, Th and Sm contents, the platinum capsules were removed after the He analyses. The apatite grains were dissolved in a 4% HNO₃ + 0.05% HF acid mixture in Savillex teflon vials, while the zircon grains were dissolved in a pressurized teflon bomb with a mixture of double-distilled 48% HF and 65% HNO₃. The dissolved crystals were spiked with calibrated ²³⁰Th and ²³³U solutions and analyzed by the isotope dilution method either on a Perkin Elmer Elan DRC II, or by a Thermo iCAP Q ICP-MS, equipped with an APEX micro-flow nebulizer. F₇-correction (alpha-ejection correction) was applied to the raw

(U–Th)/He ages according to the procedures described by Farley et al. (1996) and Hourigan et al. (2005).

The (U–Th)/He analyses were carefully evaluated sample by sample. Grains were excluded if the He re-extract exceeded 5%, if the total analytical uncertainty exceeded 10%, or if they were statistical outliers compared to the remaining single-grain analyses from the same sample according to the Grubbs and Dixon tests (Grubbs, 1950, 1969; Dixon, 1953). The excluded grains are reported together with the remaining analyses in Table 3 but are given in gray and italic. The excluded grains are not included in any figures, calculations or the thermal modelling.

5. Results

The results of the fission track and (U–Th)/He analyses are summarized in Tables 2 and 3, and shown in Figs. 3, 4 and 5. AFT single-grain ages and measured track lengths, with corresponding Dpars, and track length distributions are reported in the supplementary material (S1, S2 and S3).

5.1. Apatite fission track analyses

The 34 samples selected for apatite fission track analyses contained apatite of variable quality, including both very good and very poor grains. The apatite grains show mostly a relatively homogenous uranium distribution, with calculated uranium concentrations ranging from 3 to 52 ppm. The average Dpars, which are used as a proxy for apatite annealing kinetics, range from 1.18 μm to 1.80 μm, with most of the Dpars being below 1.5 μm. Apatite grains with such Dpars are typical fast-annealing, near-end-member fluorapatites (Carlson et al., 1999).

The apatite fission track central ages range from c. 310 to 90 Ma, but are dominated by Cretaceous (n = 20) and Triassic (n = 6) ages. Five of the samples (Table 2) failed the χ² homogeneity test (χ² < 5%; Galbraith, 2005), indicating that the dispersion of single-grain ages is larger than

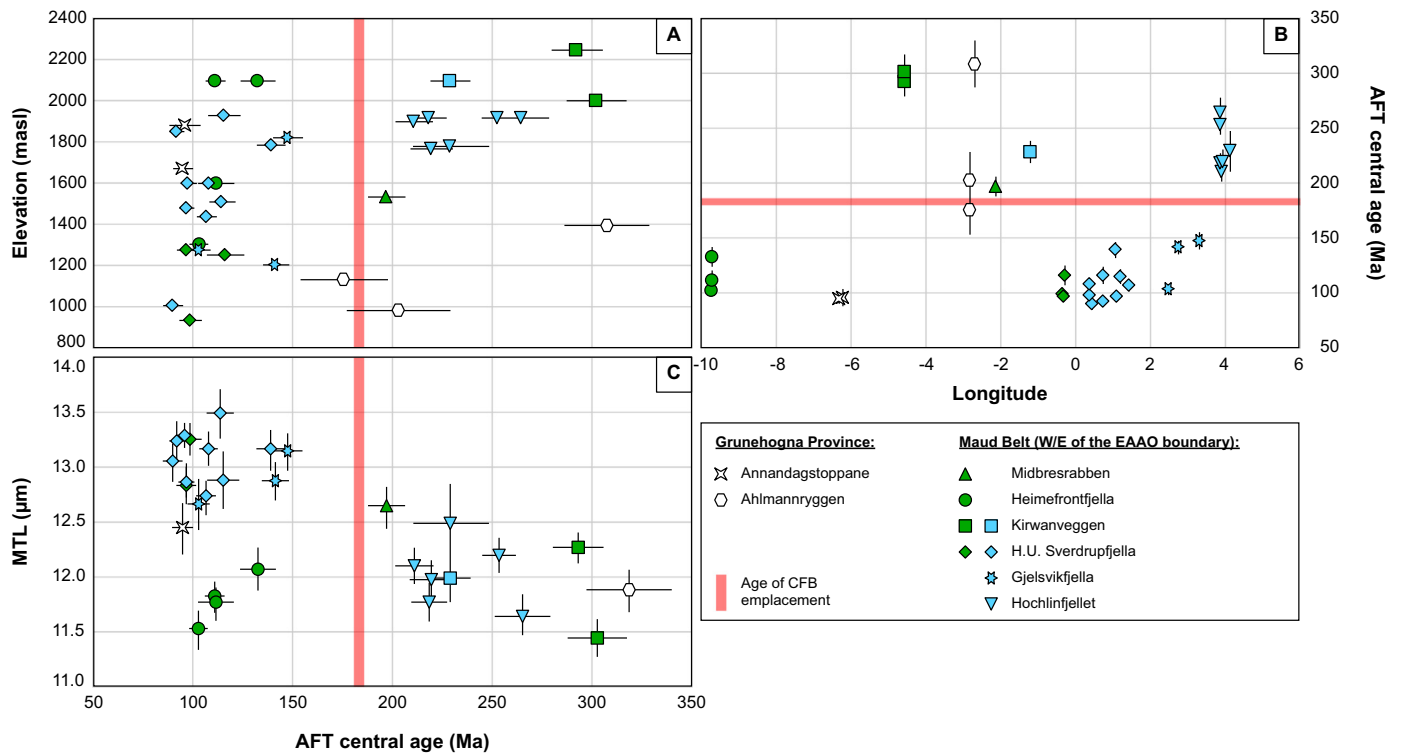


Fig. 3. Thirty-four apatite fission track ages from eight distinct regions. Error bars for AFT ages are 1σ, while error bars for mean track lengths (MTL) are 1SE. A) The age–elevation plot shows that most samples older than the continental flood basalts were collected from elevations ≥1400 masl. B) Age–longitude plot showing the strong geographic variability of AFT ages. The oldest ages occur along the flanks of Jutulstraumen–Penckgraben at Kirwanveggen, Ahlmannryggen and Midbresrabben, as well as at Hochlinfjellet, furthest to the east. East of Jutulstraumen, AFT samples generally show an eastward increase in age from H.U. Sverdrupfjella to Hochlinfjellet. C) The age–mean track length plot shows the left-hand end of a boomerang plot (Green, 1986), indicative of partial annealing of the fission tracks in the samples older than the continental flood basalts.

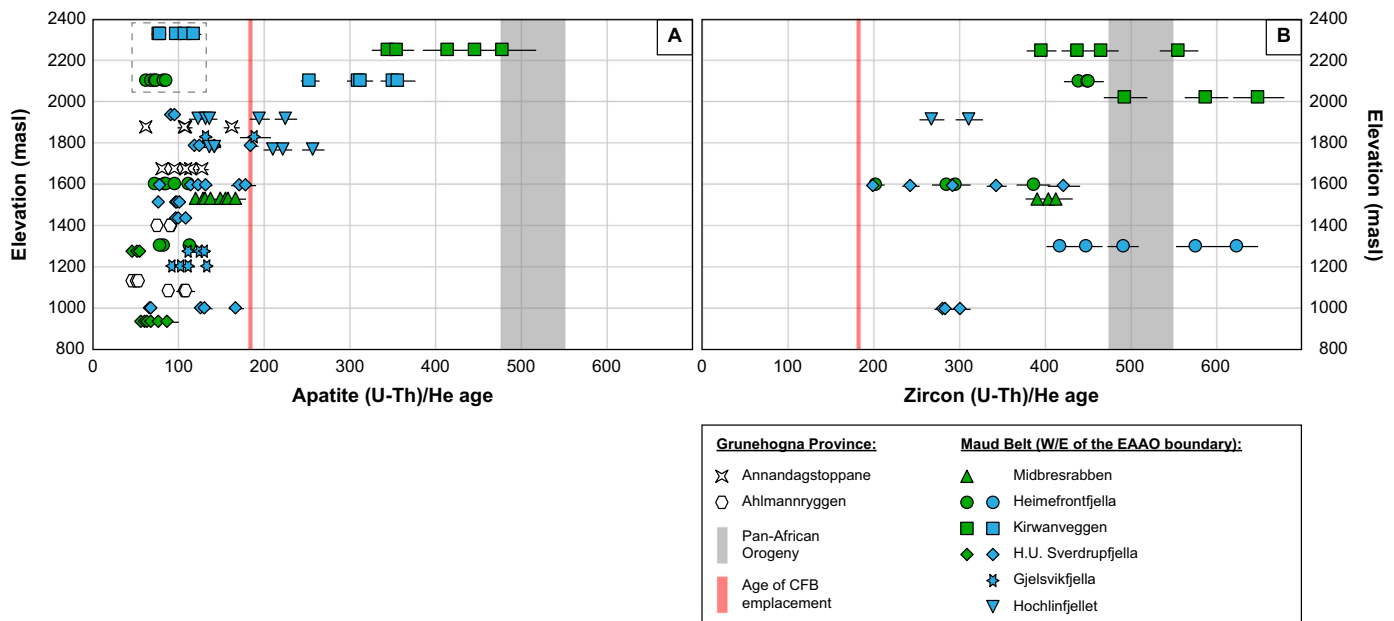


Fig. 4. Apatite and zircon (U–Th)/He ages plotted against elevation. Error bars are 1 σ . A) Apatite (U–Th)/He single-grain ages plotted against elevation scatter from late Ordovician to Eocene. With the exception of two dropstone samples from Heimefrontfjella and one Jurassic syenite sample from northern Kirwanveggen, outlined by a gray, dashed line, a strong age–elevation correlation with a break-in-slope at c. 1800 masl can be observed. This indicates that the effect of the thermal resetting by the basalts decreases with increasing elevation. B) All ZHe ages predate the Jurassic continental flood basalts, indicating that the basalts were not thick enough to reset the zircon (U–Th)/He system.

expected for a single age population. Measured mean track lengths vary from 11.4 μm to 13.5 μm .

The age–elevation plot (Fig. 3A) shows that most of the samples that are older than the Jurassic flood basalts were collected at elevations above c. 1400 masl. In addition, the AFT ages show a strong regional correlation. This is evident when plotting age against longitude, especially east of Jutulstraumen (Fig. 3B). The AFT ages increase from c. 90 Ma in H.U. Sverdrupfjella to c. 145 Ma at Gjelsvikfjella, whereas all AFT ages from Hochlinfjellet predate the continental flood basalts and cluster between 265 and 210 Ma. The age–track length plot (Fig. 3C) resembles the left-hand end of a boomerang plot (Green, 1986). Together with the broader track length distributions for samples predating the continental flood basalts (Supplementary S3; Gleadow et al., 1986), this may indicate significant track annealing in samples older than c. 200 Ma.

5.2. Apatite (U–Th)/He analyses

(U–Th)/He thermochronology of apatite from 28 samples has resulted in 114 single-grain ages. The analyzed apatite grains are generally euhedral crystals of good quality. However, small inclusions occur in some of the grains. The analyzed crystals have equivalent sphere radii between 31 and 103 μm , with most grains being smaller than 70 μm . Effective uranium (eU) concentrations range from 1 to 247 ppm but are mostly below 76 ppm eU.

Six of the 114 analyses were excluded because of high He re-extract ($n = 1$), large errors ($n = 2$), or because they were statistical outliers compared to the remaining single-grain ages of the sample ($n = 3$). Additionally, one analysis was excluded because it was significantly older than all single-grain AFT ages of that sample, which might be explained by parentless He from small inclusions that were reported for this grain during grain selection.

The apatite (U–Th)/He analyses yielded a wide range of single-grain ages from 45 to 477 Ma. Even though a lot of effort was put into selecting the best quality grains from the samples, some scatter in the single-grain ages within individual samples can be expected. Accumulation of radiation damage has proven to reduce the diffusivity of He in apatites, resulting in grains with high eU yielding older ages than low-

eU grains (e.g. Shuster et al., 2006). The He retentivity in apatites is also affected by the grain size (e.g. Reiners and Farley, 2001). As large apatites have greater effective diffusion dimensions, the He retentivity of large apatites is higher than for small apatites, resulting in greater He loss and younger ages for smaller apatites. Additionally, U–Th-rich micro-inclusions, eU zonation and He-implantation from neighboring grains can affect the age so that similar grains from the same sample can yield different (U–Th)/He ages despite having experienced a similar t – T history (Farley, 2000; Reiners and Farley, 2001; Flowers and Kelley, 2011).

The spread in the single-grain ages within a sample can be described by the standard deviation of the single-grain ages. In this study 11 samples show a standard deviation below 10%, nine samples have standard deviations between 10% and 15%, four samples show a standard deviation between 15% and 20%, while four samples have standard deviation of the single-grain ages exceeding 20%. In cases where the spread of ages cannot be explained by age–grain size or age–eU relationships, Flowers and Kelley (2011) suggest that samples with one sigma standard deviation >20% should be excluded from thermochronological modelling. For this sample suite, two of the samples with a standard deviation of the single-grain ages above 20% show a weak correlation between age and eU (H-10 and Z7.11.4), while one sample shows a strong, positive age–grain size relationship (Z7.29.10). The apatite (U–Th)/He analyses from these three samples have therefore been included in the modelling; only one sample with a high standard deviation that could not be explained by age–eU or age–grain size relationships was excluded from modelling (Z7.25.1).

The youngest AHe ages are found within Ahlmannryggen and the Jurassic syenite intrusions of Straumsvola, whereas the oldest single-grain ages were obtained from Kirwanveggen. With the exception of two granite dropstone samples from Heimefrontfjella and one sample from the c. 172 Ma syenite intrusion of Sistefjell in northern Kirwanveggen (Harris et al., 2002), the age–elevation plot (Fig. 4A) shows a strong age–elevation correlation with a break-in-slope at c. 1800 masl. The samples that postdate the Jurassic continental flood basalts are found in entire western DML, whereas the samples predating the basalts are derived from high elevations in Kirwanveggen and Hochlinfjellet.

5.3. Zircon (U–Th)/He analyses

The (U–Th)/He analyses of nine samples have resulted in 32 single-grain zircon ages. The equivalent sphere radii of the analyzed zircons range from 30 to 73 μm. The zircons are mostly characterized by effective uranium (eU) concentrations from 68 to 600 ppm, but eU concentrations up to 1481 ppm are recorded.

The zircon (U–Th)/He analyses yield Neoproterozoic to Triassic single-grain ages (c. 650–200 Ma). The data show two distinct groups of Permian and Ordovician age, respectively. The zircon (U–Th)/He ages correlate poorly with elevation (Fig. 4B). In addition, all zircon (U–Th)/He single-grain ages predate the Jurassic continental flood basalts, indicating that the temperatures below the basalts cannot have been sufficient for thermal resetting of the zircon (U–Th)/He system.

None of the single-grain (U–Th)/He analyses were rejected according to the filtering criteria specified in Section 4.2. For the majority of the samples, the standard deviation of the single-grain ages is between 1 and 15%. Two samples, however, have standard deviations above 20% (Z7.25.1: 26%; K1-1: 22%). Z7.25.1 shows a moderate, negative correlation with eU, whereas no age–eU or age–grain size relationships are present for sample K1-1. As opposed to apatites, zircons can show both positive and negative correlations between age and eU (Guenther et al., 2013). The ZHe data from sample Z7.25.1 are therefore included in the modelling.

5.4. Evaluation of the dataset

The apatite fission track single-grain ages, and thus also the AFT central ages, can be sensitive to both grain selection and counting area within the grain. Individual counting behavior by the analyst should be corrected by the zeta calibration technique (Hurford and Green, 1983). To check the reproducibility of our ages, seven randomly selected samples were analyzed independently by both A. K. Ksienzyk and H. Sirevaag. The results show excellent reproducibility, with all AFT central ages overlapping within 1σ errors (Table 2).

Combining apatite fission track data with apatite and zircon (U–Th)/He data has proven to be a useful method for constraining the cooling history from c. 230 °C to c. 35 °C. Based on the closure temperatures of the different systems, we expect the ZHe age to be oldest, and the AHe age to be the youngest in a multidated sample (e.g. Gleadow and Duddy, 1981; Farley and Stockli, 2002; Reiners et al., 2002; Shuster et al., 2006; Guenther et al., 2013). In the present dataset, all single-grain ZHe ages are older than the corresponding AFT central ages as expected (Fig. 5). However, eleven samples yield older unweighted average AHe ages than AFT central ages, although all of these AHe ages overlap with the corresponding AFT ages within 2σ standard deviation.

AFT–AHe age inversions are relatively common and have also been documented in central Dronning Maud Land (Emmel et al., 2007). The presence of fluid- or U–Th-rich micro-inclusions, He-implantation and eU zonation with U–Th-rich cores, can result in older AHe ages than

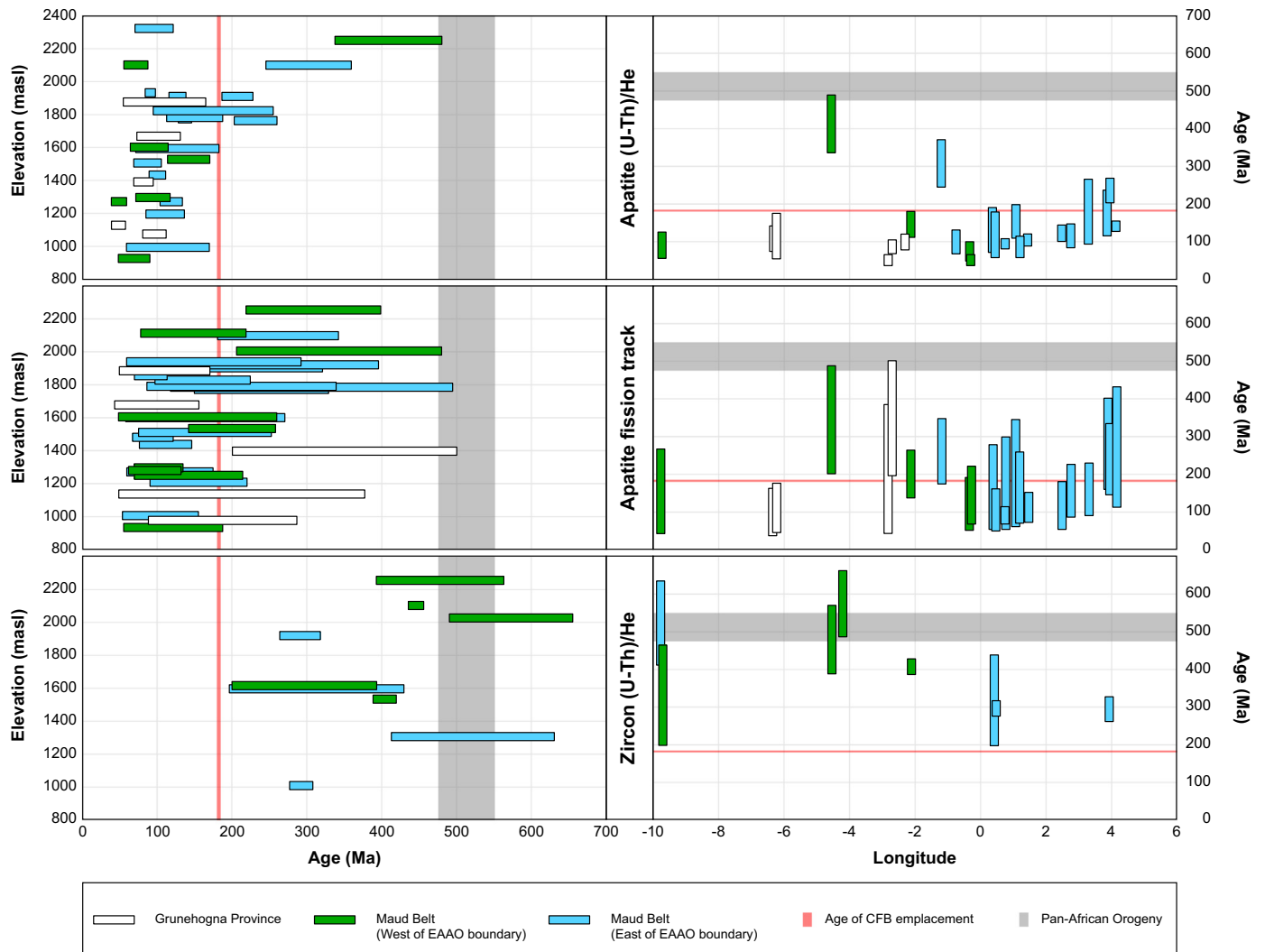


Fig. 5. Age–elevation and age–longitude plots for all thermochronological data. The bars represent the span of single-grain ages without error for the different localities.

expected, even older than the corresponding AFT age (Farley, 2002; Fitzgerald et al., 2006; Flowers and Kelley, 2011). The helium trapping model suggests that apatite becomes more He retentive with increasing radiation damage, resulting in a higher closure temperature for helium retention in apatites (Shuster et al., 2006). In our study, we apply a modified version of the helium trapping model: the radiation damage accumulation and annealing model, which uses the effective fission track density rather than He concentration as a proxy for the radiation damage (Flowers et al., 2009). By applying this model, it should therefore be possible to also model inverted AFT and AHe ages.

6. Modelling

Thermal history modelling was done with HeFTy v. 1.9.1 (Ketcham, 2016). During modelling of AFT data, the annealing model of Ketcham et al. (2007b) was applied, while the confined tracks were c-axis projected according to Ketcham et al. (2007a). For modelling of the (U–Th)/He analyses, the model of Guenther et al. (2013) and the radiation damage accumulation and annealing model of Flowers et al. (2009) were used for zircon and apatite, respectively. For samples including multiple thermochronometers, the different thermochronometers were generally modelled together. However, as discussed above, (U–Th)/He single-grain ages that showed over-dispersion which could not be explained by either variation in grain size or eU were excluded from modelling. Also, if adding (U–Th)/He data precluded the models from finding any good or acceptable paths, the different thermochronometers were tested individually, and the “problematic” thermochronometer was excluded from the modelling. The included thermochronometers are specified for each model.

For each inverse model, 100,000 random paths were run. For comparison of the different models, we use the weighted mean and best-fit paths of the acceptable (goodness-of-fit ≥ 0.05) and good (goodness-of-fit ≥ 0.5) paths. Goodness-of-fit is calculated using the Kuiper's Statistics in HeFTy (Ketcham, 2016).

The thermal models are based on pre-existing geological and thermochronological information. For the present study, we have used the following external t – T constraints:

- **Start:** In the northern part of the Maud Belt, titanite fission track ages (partial annealing zone: 265–310 °C) have been used as the starting point. Emmel et al. (2009) reported titanite fission track ages of 516 ± 50 Ma for Hochlinfjellet and 345 ± 25 Ma for areas further west. In the southern Maud Belt, temperatures of 300–350 °C are recorded by biotite and muscovite K–Ar data (Jacobs et al., 1995). The parts of the Maud Belt that were overprinted by the Pan-African East African–Antarctic Orogeny (east of the Heimefrontfjella Shear Zone) cooled below these temperatures at 505 ± 29 Ma, whereas the non-overprinted part of the Maud Belt last experienced similar temperatures at 974 ± 14 Ma (Jacobs et al., 1995). The starting point of the individual models has been set according to the thermochronological constraints from the respective area.
- **Permian peneplanation:** The presence of Permo-Carboniferous sediments deposited on a peneplain in Heimefrontfjella and Kirwanveggen indicates that basement rocks of the study areas were located close to the surface during Permian times (Jacobs et al., 1995; Jacobs and Lisker, 1999). A similar paleosurface in Gjelsvikfjella and western Mühlig-Hofmannfjella is interpreted to be of the same age (Näslund, 2001). The presence of glacial deposits in Heimefrontfjella indicate low temperatures during Early Permian times (e.g. Bauer, 2009), thus we have chosen a surface temperature of -10 °C to reflect these conditions. However, the temperature range for the modelling constraints in the Permian have been adjusted for individual samples, according to the vertical distance between the sample location and the peneplain, assuming a geothermal gradient of 25 °C/km. The same approach was followed for all constraints discussed below, accordingly.
- **Beacon sedimentation:** Up to c. 160 m of Beacon sediments are preserved in Heimefrontfjella, Kirwanveggen and Fossilryggen, whereas the corresponding Upper Carboniferous–Triassic Victoria Group is preserved in thicknesses up to c. 3 km within the Transantarctic Mountains (Isbell, 1999), far away. As we would expect that these sediments have in part been eroded in DML and may have been similarly thick as they still are in the Transantarctic Mountains, we allow for reheating by up to c. 100 °C during Beacon sedimentation. Models of the Triassic climate have suggested surface temperatures up to c. 25 °C (Wilson et al., 1994), and therefore all post-Permian surface temperatures have been set to this temperature.
- **Early Jurassic surface exposure:** At Bjørnnutane (Fig. 2), the crystalline basement is unconformably overlain by 2 m of Beacon sediments with Jurassic flood basalts on top (Juckes, 1972; Bauer, 2009). This indicates that most of the sediments were eroded and the peneplain was located close to the surface again just prior to basalt emplacement.
- **Jurassic reheating:** As 400–>1000 m of Jurassic continental flood basalts are present in Vestfjella (Luttinen and Furnes, 2000; Luttinen et al., 2015), and up to c. 5 km of Jurassic flood basalts are preserved in the Sabie River Basalt Formation in the Lebombo Monocline (Cleverly and Bristow, 1979), we allow the models to reheat during Early–Middle Jurassic times. Maximum temperatures are set to 300 °C since neither titanite fission track ages in the northern Maud Belt, nor mica K–Ar ages in the southern Maud Belt show any indication of Jurassic resetting.
- **End:** The present-day surface temperature (c. -25 °C) was used as the final constraint of the modelling.

As different starting points are used for the different areas, only the last 300 Ma are shown in the thermal models.

7. Discussion

7.1. Extent and thickness of the continental flood basalts

The age distribution maps (Fig. 6) show strong regional variations of the AFT and AHe ages, with the youngest ages located in H.U. Sverdrupfjella, Heimefrontfjella and Annandagstoppane, and the oldest ages in Kirwanveggen and Hochlinfjellet. Additionally, Paleogene AHe ages are recorded at Ahlmannryggen. No regional correlation could be observed in the ZHe data. All ZHe ages predate the Jurassic continental flood basalts, whereas both pre- and post-Jurassic apatite fission track and (U–Th)/He ages are present. Thermal models based on apatite fission track and (U–Th)/He data can therefore be useful for investigating the effect of the Jurassic basalts (Fig. 7).

Jurassic dikes are abundant in most parts of western Dronning Maud Land (Fig. 8). The number of Jurassic dikes strongly decreases east of H.U. Sverdrupfjella, and the easternmost dikes in western Dronning Maud Land are reported from Hoggstabben, north of Hochlinfjellet (Owada et al., 2003). Hydrothermal circulation, often associated with dike intrusions, can result in fission track annealing (e.g. Steckler et al., 1993). We cannot rule out local effects of hydrothermal circulation in western Dronning Maud Land, but this cannot explain Jurassic fission track annealing that is as widespread as it is observed in the study area, especially since most samples were collected well away from the basaltic dikes. The additional basaltic overburden that resulted from basalt eruption is the more likely explanation for the Jurassic heating that can be observed in our dataset. The >1000 m thick basalts that are still preserved in Vestfjella support this interpretation. We neglect the effect of direct heating from the basalts to the underlying rocks as we would expect rapid subaerial cooling of the basalts, and because the majority of the samples were not located close enough to the surface at the time of emplacement. For the following interpretations, only thermal models that yield representative t – T paths are discussed (Fig. 7, Supplementary S4a and S4b).

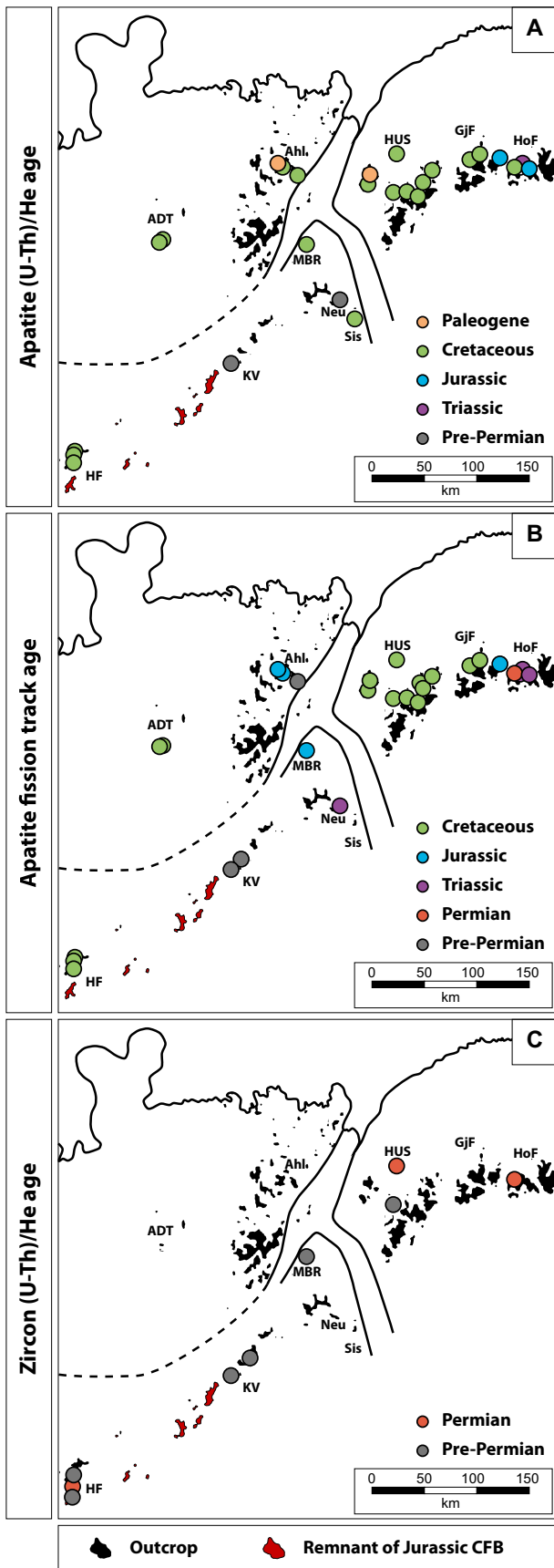


Fig. 6. Distribution of thermochronological data from western Dronning Maud Land. In A and C, the unweighted mean (U–Th)/He age is used. Abbreviations: ADT – Annandagstoppane; Ahl – Ahlmannryggen; GjF – Gjelsvikfjella; HF – Heimefrontfjella; HoF – Hochlinfjellet; HUS – H.U. Sverdrupfjella; KV – Kirwanveggen; MBR – Midbresrabben; Neu – Neumayerskarvet; Sis – Sistefjell.

7.1.1. Post-continental flood basalt samples

Samples with apatite fission track and (U–Th)/He ages that postdate the continental flood basalts comprise, by far, the largest group of samples in western Dronning Maud Land. Early–Middle Cretaceous AFT ages are mostly recorded in Heimefrontfjella, H.U. Sverdrupfjella and Gjelsvikfjella (Fig. 6B). The predominance of Cretaceous AFT and AHe ages in combination with relatively long track lengths, suggest that these ages represent cooling ages after total resetting during a Jurassic or Early Cretaceous thermal event. The widespread presence of Jurassic dykes and erosional remnants of Jurassic flood basalts as opposed to the total lack of Jurassic or Cretaceous sedimentary rocks, either in situ or in moraines, leads us to believe that this resetting of the AFT and AHe ages was caused by burial under Jurassic continental flood basalts, rather than burial by Jurassic–Cretaceous sedimentation.

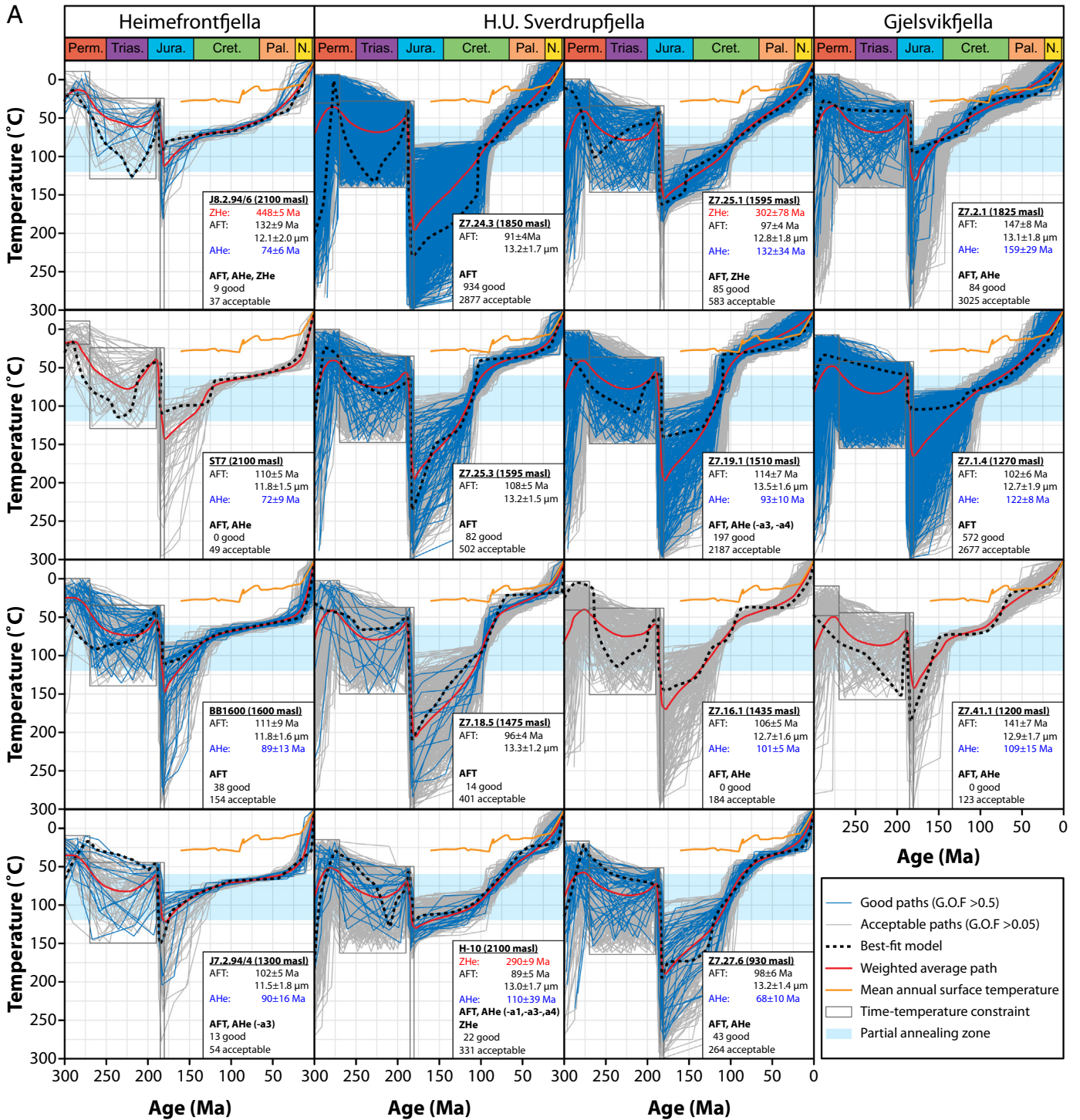
7.1.1.1. Heimefrontfjella. The four samples from Heimefrontfjella are derived from a nearly vertical profile, in which the two uppermost samples were collected a few meters above the Permian peneplain (dropstones from the base of the Beacon sediments). Thus, these two samples provide precise temperature constraints during the Permian as they must have resided at the surface at that time. Thermal modelling for samples from Heimefrontfjella (Fig. 7) indicates that the samples reached at least c. 80–90 °C during the Jurassic. Since the AFT system was essentially completely reset, maximum temperatures are poorly constrained in the models that are lacking ZHe data. The uppermost sample, which also includes ZHe data, limits the maximum temperature to c. 195 °C. The weighted mean path for this specific sample indicates Jurassic temperatures of c. 115 °C, and we consider this to be the most reliable temperature estimate for Heimefrontfjella.

7.1.1.2. H.U. Sverdrupfjella. The predominance of mid-Cretaceous AFT ages in H.U. Sverdrupfjella indicates that this region was exhumed through the apatite partial annealing zone at c. 100 Ma after total track annealing. The apatites only started to retain tracks in mid-Cretaceous times and thus the AFT data alone are unsuitable to constrain Jurassic and earlier temperature histories. All thermal models from H.U. Sverdrupfjella indicate temperatures of at least c. 85–95 °C during the Jurassic (Fig. 7). Again, the maximum Jurassic temperatures are best constrained by models that include ZHe data, as they are sensitive to reheating above the apatite partial annealing zone. Two of the models include both apatite and zircon (U–Th)/He data together with apatite fission track data, resulting in a well-constrained post-Jurassic thermal evolution. These two models indicate Jurassic temperatures up to c. 170–210 °C, resulting in weighted average temperatures of c. 130 °C and c. 155 °C, for samples H-10 and Z7.25.1, respectively.

7.1.1.3. Gjelsvikfjella. Located further east, somewhat older AFT ages were obtained from two of the samples. Previously, Jurassic AFT ages have been reported from Risemédet in Gjelsvikfjella. These ages were interpreted as being the result of marginal volcanic activity at the eastern boundary of the Bouvet–Karoo mantle plume (Emmel et al., 2009). The relatively long track lengths and the predominance of post-continental flood basalt single-grain AFT ages (Fig. 5) clearly indicate a high degree of Jurassic annealing and subsequent rapid cooling through the apatite partial annealing zone. This is also supported by the three models from Gjelsvikfjella which all show reheating up to at least c. 80–90 °C (Fig. 7). Since ZHe data are lacking from Gjelsvikfjella, we do not attempt to constrain maximum temperatures during the Jurassic.

7.1.2. Pre-continental flood basalt samples

In western Dronning Maud Land, AFT and AHe ages that predate the flood basalts are mainly found at Hochlinfjellet, Kirwanveggen and Midbresrabben, whereas pre- to syn-continental flood basalt AFT ages are found at Ahlmannryggen. The localities of these samples are in fact interesting, as these areas are located adjacent to or in-between areas comprising significantly younger AFT ages. The mean track lengths of



<p>Heimefrontfjella:</p> <ul style="list-style-type: none"> - Jurassic reheating to c. 115 °C. - Max. preferred CFB thickness: c. 1.5 km. <p>Cooling:</p> <ul style="list-style-type: none"> - M. Jur. - E. Cret.: c. 0.5 - 1.3 °C/Myr. - Cretaceous: 0.2 - 0.5 °C/Myr. - Since Paleogene: c. 1.6 - 2.4 °C/Myr. 	<p>H.U. Sverdrupfjella:</p> <ul style="list-style-type: none"> - Preferred models (H-10 and Z7.25.1) show reheating to c. 130 °C. - Maximum preferred CFB thicknesses: 1.3 - 2.0 km. <p>Cooling:</p> <ul style="list-style-type: none"> - Preferred models indicate cooling rates of c. 0.5 - 0.9 °C/Myr until mid-Cretaceous. - All models show cooling rates of c. 0.7 - 1.7 during mid- to Late Cretaceous times. - Since Paleogene times: 0.9 - 1.6 °C/Myr. 	<p>Gjelsvikfjella:</p> <ul style="list-style-type: none"> - All samples record total annealing (T > 120 °C), and max. T cannot be determined. - Minimum CFB thickness: 400 - 600 m. <p>Cooling:</p> <ul style="list-style-type: none"> - Early - mid-Cretaceous: c. 0.5 °C/Myr. - Since mid-Cretaceous: 0.7-1.0 °C/Myr.
--	--	--

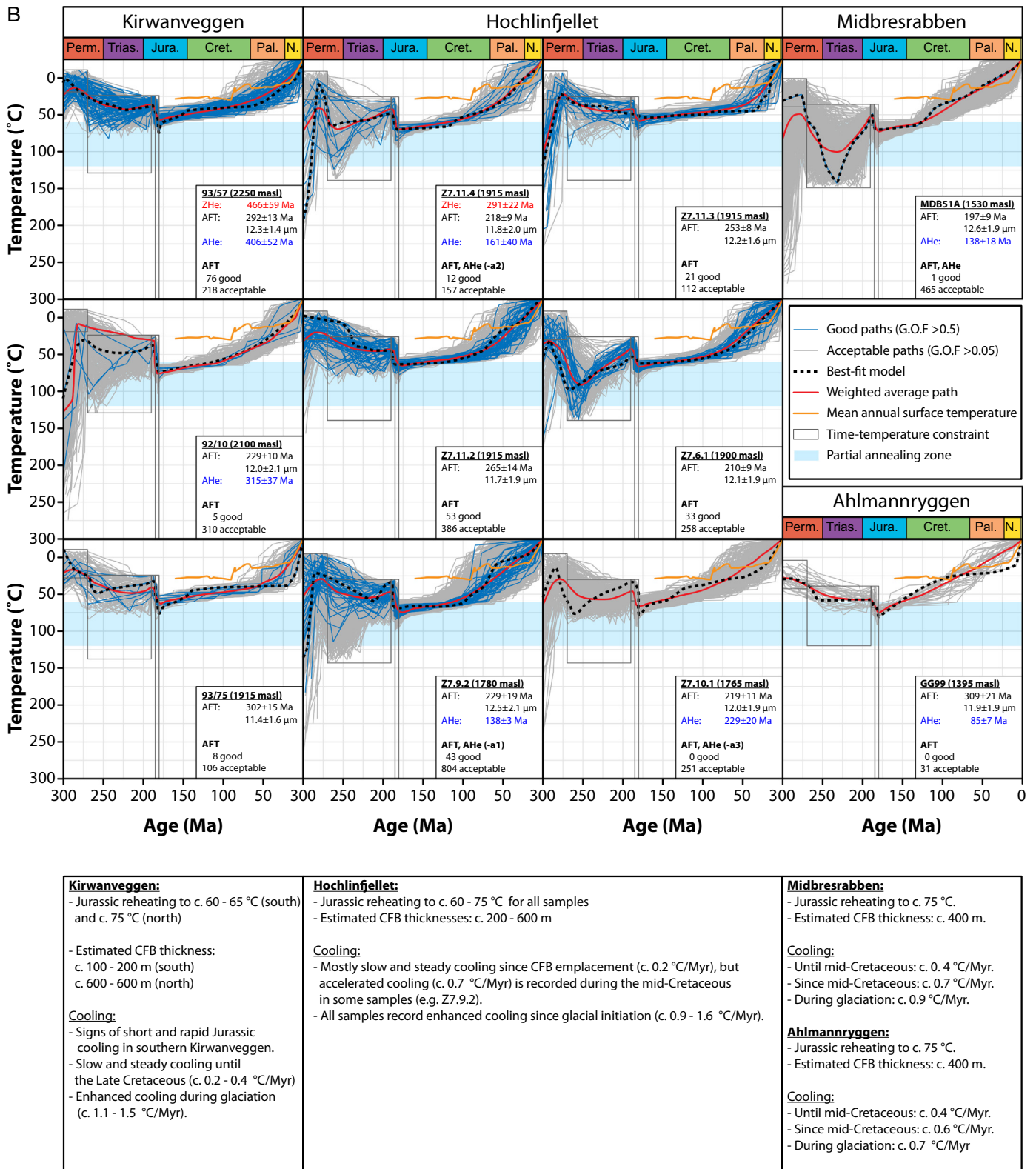


Fig. 7. HeFTy time-temperature thermal models. For each model, 100,000 random paths were tested. For each model, ZHe (red) and AHe (blue) ages are given as unweighted mean ages and 1σ error below the sample name. AFT central age and mean track length (black) are also reported with 1σ error. Below that are reported: (1) In bold, the thermochronometers included in the modelling; numbers in brackets refer to single-grain AHe analyses excluded from the modelling. (2) The number of good fit and acceptable fit paths found for each model. Good fits correspond to goodness-of-fit ≥0.5, while acceptable fits represent goodness-of-fit ≥0.05. (For interpretation of the references to colour in this figure legend, the reader is referred to the web version of this article.) Mean annual surface temperatures after Barrett (1999), Poole et al. (2005), Thorn and DeConto (2006) and Jenkyns et al. (2012).

the samples that yield these ages are shorter than in most of the samples with post-continental flood basalt apatite fission track ages (Fig. 3C). The combination of shortened fission tracks and the broader track length distributions (Supplementary S3), indicate partial annealing of the fission tracks at Kirwanveggen, Hochlinfjellet, Ahlmannryggen and Midbresrabben.

7.1.2.1. Hochlinfjellet. All samples from Hochlinfjellet yield Permo-Triassic AFT ages. All thermal models indicate minimum temperatures of c. 45–60 °C and maximum temperatures of c. 85–100 °C during the Jurassic, resulting in weighted average temperatures of c. 60–75 °C. This indicates only partial annealing, and as none of the temperature estimates are above the apatite partial annealing zone, ZHe data are not required for constraining the maximum temperatures during the Jurassic.

7.1.2.2. Kirwanveggen. At Kirwanveggen, the two multidated samples both deviate from the normal AFT–AHe age relationship. It has been suggested that inversion of AFT and AHe ages could be attributed to shock heating (e.g. Stockli et al., 2000), but it is likely that this will have an effect only within the uppermost cm of the affected rocks. As there is a difference of c. 250 m between the uppermost and lowermost samples in southern Kirwanveggen, it is not likely that the effect of short-lived heating from the lava flow could have reached the lowermost sample. Instead, we suggest that the age inversion is a cumulative result of radiation damage, U- and Th-zonation and possibly other

factors that are discussed in Section 5.4. The thermal models from Kirwanveggen vary with respect to the Jurassic reheating: The two samples from southern Kirwanveggen record temperatures of c. 40–75 °C and c. 50–85 °C for samples 93/57 and 93/75, respectively. This results in weighted average temperatures of c. 60–65 °C for the two samples. Sample 92/10 from northern Kirwanveggen records higher temperatures of 65–105 °C, with a weighted average temperature of c. 75 °C.

7.1.2.3. Ahlmannryggen and Midbresrabben. The samples from Ahlmannryggen and Midbresrabben were derived from opposite sides of the Jutulstraumen and their track length distributions and thermal models show similarities with respect to the degree of fission track annealing during the Jurassic. Midbresrabben probably reached temperatures of c. 60–105 °C, whereas the model from Ahlmannryggen indicates Jurassic temperatures between c. 65 °C and 95 °C. This results in weighted average temperatures of c. 75 °C at both localities.

7.1.3. Estimation of basaltic thicknesses

A thick layer of continental flood basalt is usually associated with high geothermal gradients. For the 65 Ma Deccan continental flood basalts in India, a geothermal gradient of c. 35–80 °C/km has been estimated (Negi et al., 1993). For simplicity, the following thickness estimates are based on the difference in pre- and post-emplacment temperatures, using a geothermal gradient of 50 °C/km. It has to be pointed out, however, that for most samples the pre-emplacment temperatures are not constrained by the data (since most samples

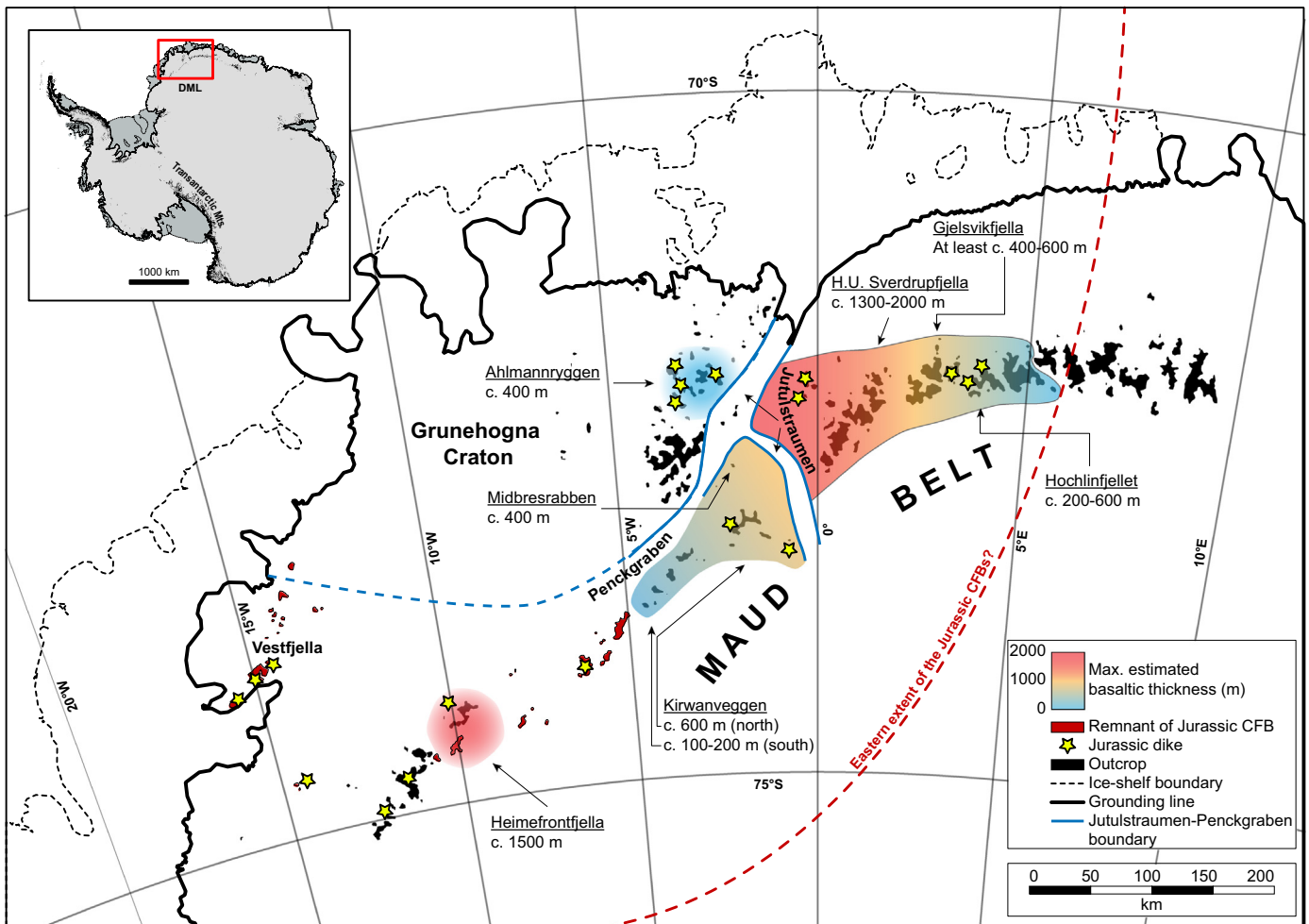


Fig. 8. Summary of estimated thicknesses of the Jurassic continental flood basalts in western Dronning Maud Land.

Jurassic dikes after Furnes and Mitchell (1978), Furnes et al. (1982), Grantham et al. (1988), Harris et al. (2002), Luttinen et al. (2002), Owada et al. (2003), Zhang et al. (2003), Riley et al. (2005), Curtis et al. (2008) and Spaeth (2009).

experienced total annealing during basalt emplacement), but rather by the external constraints, i.e. the requirement that samples were at or close to the surface, depending on their depth below the peneplain and the thickness of the remaining Beacon sediments. We assume that the weighted mean path is representative for the pre-emplacment temperature, but this involves some elements of uncertainty. A summary of estimated thicknesses is given in Fig. 8.

7.1.3.1. Completely annealed regions. Heimefrontfjella, H.U. Sverdrupfjella and Gjelsvikfjella are all characterized by total apatite fission track annealing during the Jurassic. By comparing the temperatures prior to and just after continental flood basalt emplacement in the models from Heimefrontfjella, an increase in temperatures of at least c. 30 °C is recorded for all samples, corresponding to basaltic thicknesses of at least c. 600 m. However, we prefer the estimate from sample J8.2.94/6 as ZHe data allow us to properly constrain the maximum temperature. The weighted mean path from this specific sample indicates heating by c. 75 °C, corresponding to c. 1.5 km of basalts. Previous thermochronological studies from Heimefrontfjella have suggested that this region was covered by 1.5–2.0 km of basalts (e.g. Jacobs and Lisker, 1999), and this is therefore confirmed by our estimates.

All thermal models from H.U. Sverdrupfjella show an increase in temperatures of at least c. 20 °C. The weighted mean path of the two models including ZHe data, H-10 and Z7.25.1, indicate heating by c. 65–100 °C, to maximum temperatures of c. 130–155 °C. Consequently, the thickest basaltic cover in western Dronning Maud Land was most likely located in H.U. Sverdrupfjella, corresponding to c. 1.3–2.0 km.

In Gjelsvikfjella, a temperature increase of at least c. 20–30 °C is shown in the thermal models, corresponding to minimum basaltic thickness of c. 400–600 m. Due to the lack of ZHe data and the total annealing of the AFT data, the maximum temperatures cannot be constrained from Gjelsvikfjella in the current dataset. However, as the continental flood basalts were emplaced through the lithospheric thinning zones of Jutulstraumen–Penckgraben and Mozambique–Weddell Sea (Luttinen and Furnes, 2000), we would expect diminishing thicknesses of the basalts away from the emplacement zone. Thus, we speculate that the maximum thicknesses at Gjelsvikfjella should be lower than in H.U. Sverdrupfjella, and higher than at Hochlinfjellet.

7.1.3.2. Partially annealed regions. The thermal models from Hochlinfjellet, Kirwanveggen, Ahlmannryggen and Midbresrabben indicate weighted average temperatures of c. 60–75 °C during basalt emplacement. This shows that the basalts did not reach thicknesses sufficient for total track annealing.

The thermal models from Kirwanveggen show an increase in temperature of at least c. 5–10 °C and c. 30 °C in southern and northern Kirwanveggen, respectively. This corresponds to thicknesses of c. 100–200 m and 600 m. The temperatures of Ahlmannryggen and Midbresrabben increased at least c. 5–10 °C during basalt emplacement, but the weighted mean paths indicate an increase in temperature of c. 20 °C for both samples. This temperature difference corresponds to basaltic thicknesses of c. 400 m. At Hochlinfjellet, a difference of c. 10–30 °C is recorded between the pre- and syn-emplacment temperatures, corresponding to c. 200–600 m difference in cover. Generally, basaltic layers are good insulators with high geothermal gradients, but it is possible that such a thin layer would reduce the insulation, and therefore also lower the geothermal gradient. Our thickness estimates are based on a geothermal gradient of 50 °C/km and might underestimate the true thickness if geothermal gradients were indeed lower.

Previous work has suggested that Gjelsvikfjella further west was affected by marginal volcanic activity (Emmel et al., 2009). Together with the presence of Jurassic dikes at Hoggstabben, our data from Hochlinfjellet clearly indicate Jurassic reheating further east than previously suggested, and at least as far east as c. 4°E (Fig. 8). We suggest that the reason for the eastward diminishing thermal influence from the

continental flood basalts is related to the distance from the zone of emplacement in Jutulstraumen–Penckgraben.

Kirwanveggen, Ahlmannryggen and Midbresrabben are all located close to the anticipated eruption center within Jutulstraumen–Penckgraben, therefore the relatively thin basaltic cover must have a different explanation than at Hochlinfjellet. The Jurassic flood basalts of Vestfjella are low-viscosity tholeiitic lavas (e.g. Luttinen and Furnes, 2000), and such lavas of flood basalt provinces tend to fill in topographic lows. The simplest explanation for the absence of a thick pile of lavas is therefore that Kirwanveggen, Ahlmannryggen and Midbresrabben were topographic highs at the time the flood basalts erupted. This could either indicate a pre-existing topography (i.e. the Permian peneplain was not all that plane), or the topography had already been modified by early rift processes prior to the eruption of the basalts. Kirwanveggen, Ahlmannryggen and Midbresrabben are all located directly adjacent to the Jurassic Jutulstraumen–Penckgraben rift (e.g. Riley et al., 2005). It is therefore possible that these regions experienced syn-volcanic rift flank uplift, which inhibited the accumulation of continental flood basalts to thicknesses sufficient for total track annealing.

7.2. Post-continental flood basalt cooling

During basalt emplacement, variable basaltic thicknesses of up to c. 2 km were recorded in western Dronning Maud Land. Since basalt emplacement in Early Jurassic times, our data record cooling first during Jurassic–Cretaceous times, and then since the late Paleogene.

7.2.1. Jurassic–Cretaceous cooling

As all models show at least some degree of Jurassic reheating, post-Jurassic cooling is required for all samples. There are, however, some major differences between the different regions. Based on the nature of the post-continental flood basalt cooling, we have generally two types of samples: those that show accelerated cooling in the Jurassic and those that experienced enhanced cooling in the Cretaceous. Additionally, some samples from Hochlinfjellet show very slow cooling until at least Paleogene times. These will not be discussed further in this section.

The models from Heimefrontfjella and southern Kirwanveggen (samples 93/57 and 93/75) all show immediate rapid cooling just after the emplacement of the Jurassic flood basalts. In Heimefrontfjella, Jurassic cooling rates of c. 0.8–1.3 °C/Myr are recorded. This is followed by decreasing cooling rates (c. 0.2–0.5 °C/Myr) throughout the Cretaceous. Similar to the thermal models from Jacobs and Lisker (1999), our models show cooling through the apatite partial annealing zone during Late Cretaceous times. The accelerated cooling in southern Kirwanveggen is mostly recorded by the best-fit paths, but compared to Heimefrontfjella, this cooling phase is less pronounced with significantly lower cooling rates. Similar to Heimefrontfjella, the samples from southern Kirwanveggen show very slow cooling throughout the Cretaceous (c. 0.2 °C/Myr).

Thermal models from the remaining areas show, at least to some extent, accelerated cooling during the Cretaceous. This cooling phase is most pronounced in the samples from H.U. Sverdrupfjella, Midbresrabben and Gjelsvikfjella. The preferred models from H.U. Sverdrupfjella show cooling rates of c. 0.5–0.9 °C/Myr until mid-Cretaceous times. As all samples from H.U. Sverdrupfjella start to retain tracks during mid-Cretaceous times, the cooling histories since c. 100 Ma are recorded also in the samples lacking ZHe data. Mid- to Late Cretaceous cooling rates up to c. 1.7 °C/Myr record the accelerated cooling during mid-Cretaceous times in H.U. Sverdrupfjella. From Gjelsvikfjella, the cooling can only be resolved since the Early Cretaceous for one sample (Z7.41.1), showing cooling rates of c. 0.5 °C/Myr until the mid-Cretaceous. Since mid-Cretaceous times, all three models indicate slightly higher cooling rates (up to c. 1.0 °C/Myr). The Jurassic–Early Cretaceous slow cooling (c. 0.3 °C/Myr) at Midbresrabben is also

followed by accelerated cooling since mid-Cretaceous times (c. 0.7 °C/Myr).

The regional variation in cooling pattern in our models is very interesting. Our thermal models indicate initial Jurassic cooling in the NE–SW trending part of the southern Maud Belt (Heimefrontfjella, southern Kirwanveggen and possibly Ahlmannryggen), while the cooling in the E–W trending mountain range took place mostly during the Cretaceous. Similar cooling phases have previously been described in western and central Dronning Maud Land (e.g. Jacobs et al., 1992; Jacobs et al., 1995; Jacobs and Lisker, 1999; Meier, 1999; Meier et al., 2004; Emmel et al., 2009) and in southern Africa (e.g. Brown et al., 1990; Brown et al., 2002; Wildman et al., 2015; Wildman et al., 2016; Wildman et al., 2017) where it has been attributed to different phases of Gondwana rifting and the subsequent opening of the Atlantic.

The Jurassic–Cretaceous was a period of major reorganization in the vicinity of Dronning Maud Land, including the initial rifting of Gondwana, the opening of the Riiser-Larsen Sea (c. 165–135 Ma; Roeser et al., 1996), the transition from two-plate to three-plate configuration when South America was separated from Africa (e.g. Lawver et al., 1991; Storey, 1995), and the subsequent detachment of India–Sri Lanka from Antarctica (Powell et al., 1988; Lawver et al., 1991).

The Karoo mantle plume probably resulted in first dynamic, then permanent uplift of the Mesoproterozoic basement and the overlying Beacon sediments in Heimefrontfjella to elevations of c. 2 km during the initial Gondwana rifting (e.g. White and McKenzie, 1989; Jacobs and Lisker, 1999). It has been suggested that the pre-existing structures of Jutulstraumen–Penckgraben were reactivated during this rift phase (Riedel et al., 2012). It is therefore likely that the combination of these events resulted in greater relief in Heimefrontfjella and southern Kirwanveggen, promoting enhanced denudation shortly after the basalt emplacement. Due to the proximity between Heimefrontfjella, southern Kirwanveggen and the southern continuation of Penckgraben, we suggest that this is the primary explanation for the initial Jurassic cooling, whereas the subsequent Jurassic–Early Cretaceous cooling is attributed to the separation between South America and Africa (e.g. Lawver et al., 1991; Storey, 1995), and the detachment of the India–Sri Lanka block from Antarctica (Powell et al., 1988; Lawver et al., 1991).

The mid-Cretaceous cooling phase is mostly recorded in the coast-proximal samples. Throughout the Cretaceous, the passive margin development of Dronning Maud Land continued. It has been suggested that the delayed response to rifting in the South Atlantic was due to slowly cooling lithosphere, resulting from slow spreading and the vicinity to the heat source at the rift axis. The increased production of ocean floor together with the opening of the eastern Riiser-Larsen shelf and the accelerated northwards drift of India is thought to have accelerated lithosphere cooling, which eventually led to the lowering of the erosional base level (Meier, 1999). As a response to the isostatic uplift related to the passive margin development and enhanced chemical weathering due to a temperate–subtropical Cretaceous climate (Kennett and Barker, 1990), accelerated denudation and cooling took place during Middle–Late Cretaceous times in Dronning Maud Land (Meier, 1999; Meier et al., 2004).

Thus, our models record a transition from cooling associated with rifting along the NE–SW trending Jutulstraumen–Penckgraben during the Jurassic in Heimefrontfjella and southern Kirwanveggen, to the passive margin development during mid-Cretaceous times for the coast-proximal samples.

7.2.2. Late Paleogene cooling

At the onset of the 34 Ma glaciation, temperature estimates of the samples vary greatly between the different regions, with temperatures ranging from c. 0 °C to 60 °C. A prominent feature in most of the thermal models is the significant increase in cooling rates. Average cooling rates of c. 0.2–1.1 °C/Myr prevailed during Paleocene and Eocene times. Since

the Eocene–Oligocene boundary, cooling rates of 0.7–2.4 °C/Myr are recorded; the highest cooling rates are found in Heimefrontfjella (1.6–2.4 °C/Myr).

The southward drift and successive isolation of Antarctica resulted in a transition from a temperate–subtropical climate with relatively warm surface- and bottom waters (Kennett and Barker, 1990), to cooling and eventually glaciation during Eocene–Oligocene times (e.g. Ingólfsson, 2004). The transition to glacial conditions resulted in enhanced denudation, at least until Middle Miocene times. At this time, the East Antarctic ice-sheet changed from being wet-based and erosive, to cold-based, inhibiting glacial erosion (Näslund, 2001).

By comparing the weighted mean and best-fit t - T model paths with the mean annual surface temperature curve (Fig. 7), it becomes obvious that the onset of increased cooling of the basement rocks coincides with the rapidly decreasing temperatures in the Late Paleogene. Some of the cooling documented by the models might therefore be attributed simply to the cooling climate. However, many samples show a much greater temperature decrease during the Late Paleogene–Neogene than can be explained by climate deterioration. Therefore, they clearly document the increased denudation that must have accompanied the onset of the Antarctic glaciation. Even though faulting cannot be excluded as the cause of enhanced cooling, we believe that the increased cooling is due to significant glacial erosion for two reasons: Firstly, since the last phase of rifting in the Cretaceous, the continental margin outside Dronning Maud Land has been passive, suggesting relative tectonic stability. Secondly, freeze–thaw during climate change has proven to significantly enhance weathering (e.g. Yumoto et al., 2006), thus providing a very efficient erosion mechanism during the Eocene to middle Miocene.

In our thermal models, the weighted mean paths generally follow the surface temperatures since the Miocene, suggesting that most of the samples were located close to the surface already then. Our thermal models are therefore consistent with the nature of the East Antarctic ice-sheet, showing enhanced denudation until the transition from a wet-based to a cold-based ice-sheet in Miocene times.

8. Summary and conclusions

Low-temperature thermochronological data from 40 samples document the post-Pan-African thermal evolution of western Dronning Maud Land. The zircon (U–Th)/He data suggest that most parts of wDML were exhumed through temperatures of 200–230 °C, either shortly after the Pan-African orogeny or during Permian peneplanation. The apatite fission track analyses indicate an uneven distribution of continental flood basalts in western Dronning Maud Land. Post-continental flood basalt apatite fission track ages are found in Heimefrontfjella, H.U. Sverdrupfjella and Gjelsvikfjella where they document total fission track annealing due to burial of up to 2 km of flood basalts. Apatite fission track ages predating the continental flood basalts result from partial fission track annealing under a thinner basaltic cover. These ages are found at Hochlinfjellet, Kirwanveggen, Midbresrabben and Ahlmannryggen, and correspond to basaltic thicknesses of c. 100–600 m. Variation in the thickness of the basalt are attributed to the eastward diminishing thickness away from the zone of emplacement (Hochlinfjellet) and possible pre-existing topography or syn-volcanic rift flank uplift (Ahlmannryggen, Midbresrabben and Kirwanveggen). Based on the eastward diminishing thermal influence we suggest that the basalts did extend as far east as Hochlinfjellet at 4°E.

Two main phases of cooling are recorded following the emplacement of the continental flood basalts (c. 183 Ma). This includes Late Jurassic–Cretaceous cooling, associated with reactivation of the Jutulstraumen–Penckgraben rift (Riedel et al., 2012), the initial opening of the South Atlantic, major plate reorganization, and increased chemical weathering and mechanical instabilities after a protracted period of

riftling in the South Atlantic in a temperate–subtropical climate (Kennett and Barker, 1990). Finally, a phase of Early–Middle Cenozoic cooling related to the onset of glaciation is recorded. At least 2 km of denudation must have taken place since the Jurassic, as only small amounts of Jurassic continental flood basalts are preserved in western Dronning Maud Land.

Supplementary data to this article can be found online at <https://doi.org/10.1016/j.gr.2018.04.017>.

Acknowledgements

This project was funded through the PhD program at the University of Bergen and the University of Bergen Meltzer fund. H.R.M thanks the British Antarctic Survey and the Norwegian Polar Institute for logistic support during the 2007/2008 field season, and the NERC Antarctic Funding (grant NE/D008689/1, Chris Hawkesworth). We thank Geoffrey H. Grantham and Chris Harris for providing some of the samples. Judit Dunklén-Nagy and Irina Maria Dumitru are thanked for help with sample preparation and Karen Tellefsen for help with editing text and figures. We appreciate the critical reviews from Paul Green, Wilfried Bauer and an anonymous reviewer, and thank editor Toshiaki Tsunogae for handling this paper.

References

- Arndt, N.T., Todt, W., Chauvel, C., Tapfer, M., Weber, K., 1991. U–Pb zircon age and Nd isotopic composition of granitoids, charnockites and supracrustal rocks from Heimfrontfjella, Antarctica. *Geologische Rundschau* 80, 759–777.
- Barrett, P.J., 1981. History of the Ross Sea region during the deposition of the Beacon Supergroup 400–180 million years ago. *Journal of the Royal Society of New Zealand* 11, 447–458.
- Barrett, P.J., 1999. Antarctic climate history over the last 100 million years. *Terra Antarctica Reports* 3, 53–72.
- Barton, J.M., Klemd, R., Allsopp, H.L., Auret, S.H., Copperthwaite, Y.E., 1987. The geology and geochronology of the Annandagstoppane granite, Western Dronning Maud Land, Antarctica. *Contributions to Mineralogy and Petrology* 97, 488–496.
- Bauer, W., 2009. Permian sedimentary cover, Heimfrontfjella, western Dronning Maud Land (East Antarctica). *Polarforschung* 79, 39–42.
- Bauer, W., Hagemann, H., Poscher, R., Sachsenhofer, R., Spaeth, G., 1997. Permian coals from Western Dronning Maud Land: composition, environment, and the influence of Jurassic magmatism on their maturity. *The Antarctic Region: Geological Evolution and Processes*, pp. 945–951.
- Bauer, W., Siemes, H., Spaeth, G., Jacobs, J., 2016. Transpression and tectonic exhumation in the Heimfrontfjella, western orogenic front of the East African/Antarctic Orogen, revealed by quartz textures of high strain domains. *Polar Research* 35, 25420.
- Bisnath, A., Frimmel, H.E., Armstrong, R.A., Board, W.S., 2006. Tectono-thermal evolution of the Maud Belt: new SHRIMP U–Pb zircon data from Gjelsvikfjella, Dronning Maud Land, East Antarctica. *Precambrian Research* 150, 95–121.
- Board, W.S., Frimmel, H.E., Armstrong, R.A., 2005. Pan-African tectonism in the Western Maud Belt: P–T–t path for high-grade gneisses in the H.U. Sverdrupfjella, East Antarctica. *Journal of Petrology* 46, 671–699.
- Brown, R.W., Rust, D.J., Summerfield, M.A., Gleadow, A.J.W., De Wit, M.C.J., 1990. An early Cretaceous phase of accelerated erosion on the south-western margin of Africa: evidence from apatite fission track analysis and the offshore sedimentary record. *International Journal of Radiation Applications and Instrumentation. Part D. Nuclear Tracks and Radiation Measurements* 17, 339–350.
- Brown, R.W., Summerfield, M.A., Gleadow, A.J.W., 2002. Denudational history along a transect across the Drakensberg Escarpment of southern Africa derived from apatite fission track thermochronology. *Journal of Geophysical Research - Solid Earth* 107.
- Carlson, W.D., Donelick, R.A., Ketcham, R.A., 1999. Variability of apatite fission-track annealing kinetics: I. Experimental results. *American Mineralogist* 84, 1213–1223.
- Cleverly, R.W., Bristow, J.W., 1979. Revised volcanic stratigraphy of the Lebombo Monocline. *South African Journal of Geology* 82, 227–230.
- Cox, K.G., 1992. Karoo igneous activity, and the early stages of the break-up of Gondwanaland. *Geological Society, London, Special Publications* 68, 137–148.
- Curtis, M.L., Riley, T.R., Owens, W.H., Leat, P.T., Duncan, R.A., 2008. The form, distribution and anisotropy of magnetic susceptibility of Jurassic dykes in H.U. Sverdrupfjella, Dronning Maud Land, Antarctica. Implications for dyke swarm emplacement. *Journal of Structural Geology* 30, 1429–1447.
- Dalziel, I.W.D., Lawver, L.A., Norton, I.O., Gahagan, L.M., 2013. The Scotia Arc: genesis, evolution, global significance. *Annual Review of Earth and Planetary Sciences* 41, 767–793.
- DeConto, R.M., Pollard, D., 2003. Rapid Cenozoic glaciation of Antarctica induced by declining atmospheric CO₂. *Nature* 421, 245–249.
- Dixon, W.J., 1953. Processing data for outliers. *Biometrics* 9, 74–89.
- Donelick, R.A., O'Sullivan, P.B., Ketcham, R.A., 2005. Apatite fission-track analysis. *Reviews in Mineralogy and Geochemistry* 58, 49–94.
- Dumitru, T.A., 1993. A new computer-automated microscope stage system for fission-track analysis. *Nuclear Tracks and Radiation Measurements* 21, 575–580.
- Duncan, R.A., Hooper, P.R., Rehacek, J., Marsh, J.S., Duncan, A.R., 1997. The timing and duration of the Karoo igneous event, southern Gondwana. *Journal of Geophysical Research* 102, 18127–18138.
- Dunkl, I., 2002. Trackkey: a Windows program for calculation and graphical presentation of fission track data. *Computers & Geosciences* 28, 3–12.
- Emmel, B., Jacobs, J., Crowhurst, P., Daszinnies, M.C., 2007. Combined apatite fission-track and single grain apatite (U–Th)/He ages from basement rocks of central Dronning Maud Land (East Antarctica)—possible identification of thermally overprinted crustal segments? *Earth and Planetary Science Letters* 264, 72–88.
- Emmel, B., Jacobs, J., Crowhurst, P., Austegard, A., Schwarz-Schampera, U., 2008. Apatite single-grain (U–Th)/He data from Heimfrontfjella, East Antarctica: indications for differential exhumation related to glacial loading? *Tectonics* 27, 13.
- Emmel, B., Jacobs, J., Daszinnies, M.C., 2009. Combined titanite and apatite fission-track data from Gjelsvikfjella, East Antarctica – another piece of a concealed intracontinental Permo-Triassic Gondwana rift basin? *Geological Society, London, Special Publications* 324, 317–330.
- Farley, K.A., 2000. Helium diffusion from apatite: general behavior as illustrated by Durango fluorapatite. *Journal of Geophysical Research - Solid Earth* 105, 2903–2914.
- Farley, K.A., 2002. (U–Th)/He dating: techniques, calibrations, and applications. *Reviews in Mineralogy and Geochemistry* 47, 819–844.
- Farley, K.A., Stockli, D.F., 2002. (U–Th)/He dating of phosphates: apatite, monazite, and xenotime. *Reviews in Mineralogy and Geochemistry* 48, 559–577.
- Farley, K.A., Wolf, R.A., Silver, L.T., 1996. The effects of long alpha-stopping distances on (U–Th)/He ages. *Geochimica et Cosmochimica Acta* 60, 4223–4229.
- Fitzgerald, P.G., Baldwin, S.L., Webb, L.E., O'Sullivan, P.B., 2006. Interpretation of (U–Th)/He single grain ages from slowly cooled crustal terranes: a case study from the Transantarctic Mountains of southern Victoria Land. *Chemical Geology* 225, 91–120.
- Flowers, R.M., Kelley, S.A., 2011. Interpreting data dispersion and “inverted” dates in apatite (U–Th)/He and fission-track datasets: an example from the US midcontinent. *Geochimica et Cosmochimica Acta* 75, 5169–5186.
- Flowers, R.M., Ketcham, R.A., Shuster, D.L., Farley, K.A., 2009. Apatite (U–Th)/He thermochronometry using a radiation damage accumulation and annealing model. *Geochimica et Cosmochimica Acta* 73, 2347–2365.
- Fretwell, P., Pritchard, H.D., Vaughan, D.G., Bamber, J.L., Barrand, N.E., Bell, R., Bianchi, C., Bingham, R.G., Blankenship, D.D., Casassa, G., Catania, G., Callens, D., Conway, H., Cook, A.J., Corr, H.F.J., Damaske, D., Damm, V., Ferraccioli, F., Forsberg, R., Fujita, S., Gim, Y., Gogineni, P., Griggs, J.A., Hindmarsh, R.C.A., Holmlund, P., Holt, J.W., Jacobel, R.W., Jenkins, A., Jokat, W., Jordan, T., King, E.C., Kohler, J., Krabill, W., Riger-Kusk, M., Langley, K.A., Leitchenkov, G., Leuschen, C., Luyendyk, B.P., Matsuoka, K., Mouginot, J., Nitsche, F.O., Nogi, Y., Nost, O.A., Popov, S.V., Rignot, E., Rippon, D.M., Rivera, A., Roberts, J., Ross, N., Siegert, M.J., Smith, A.M., Steinhage, D., Studinger, M., Sun, B., Tinto, B.K., Welch, B.C., Wilson, D., Young, D.A., Xiangbin, C., Zirizzotti, A., 2013. Bedmap2: improved ice bed, surface and thickness datasets for Antarctica. *The Cryosphere* 7, 375–393.
- Furnes, H., Mitchell, J.G., 1978. Age relationships of Mesozoic basalt lava and dykes in Vestfjella, Dronning Maud Land, Antarctica. *Norsk Polarinstittut Skrifter* 169, 45–68.
- Furnes, H., Neumann, E.-R., Sundvoll, B., 1982. Petrology and geochemistry of Jurassic basalt dykes from Vestfjella, Dronning Maud Land, Antarctica. *Lithos* 15, 295–304.
- Furnes, H., Vad, E., Austrheim, H., Mitchell, J.G., Garmann, L.B., 1987. Geochemistry of basalt lavas from Vestfjella and adjacent areas, Dronning Maud Land, Antarctica. *Lithos* 20, 337–356.
- Galbraith, R.F., 2005. *Statistics for Fission Track Analysis*. CRC Press.
- Gleadow, A.J.W., 1981. Fission-track dating methods: what are the real alternatives? *Nuclear Tracks* 5, 3–14.
- Gleadow, A.J.W., Duddy, I.R., 1981. A natural long-term track annealing experiment for apatite. *Nuclear Tracks* 5, 169–174.
- Gleadow, A.J.W., Duddy, I.R., Green, P.F., Hegarty, K.A., 1986. Fission track lengths in the apatite annealing zone and the interpretation of mixed ages. *Earth and Planetary Science Letters* 78, 245–254.
- Golynsky, A., Jacobs, J., 2001. Grenville-age versus Pan-African magnetic anomaly imprints in Western Dronning Maud Land, East Antarctica. *The Journal of Geology* 109, 136–142.
- Grantham, G., Groenewald, P., Hunter, D., 1988. Geology of the northern H.U. Sverdrupfjella, western Dronning Maud Land and implications for Gondwana reconstructions. *South African Journal of Antarctic Research* 18, 2–10.
- Green, P.F., 1986. On the thermo-tectonic evolution of Northern England: evidence from fission track analysis. *Geological Magazine* 123, 493–506.
- Groenewald, P.B., Grantham, G.H., Watkeys, M.K., 1991. Geological evidence for a Proterozoic to Mesozoic link between southeastern Africa and Dronning Maud Land, Antarctica. *Journal of the Geological Society* 148, 1115–1123.
- Groenewald, P.B., Moyes, A.B., Grantham, G.H., Krynauw, J.R., 1995. East Antarctic crustal evolution: geological constraints and modelling in western Dronning Maud Land. *Precambrian Research* 75, 231–250.
- Grubbs, F.E., 1950. Sample criteria for testing outlying observations. *The Annals of Mathematical Statistics* 21, 27–58.
- Grubbs, F.E., 1969. Procedures for detecting outlying observations in samples. *Technometrics* 11, 1–21.
- Guenther, W.R., Reiners, P.W., Ketcham, R.A., Nasdala, L., Giester, G., 2013. Helium diffusion in natural zircon: radiation damage, anisotropy, and the interpretation of zircon (U–Th)/He thermochronology. *American Journal of Science* 313, 145–198.
- Harris, C., Marsh, J.S., Duncan, A.R., Erlank, A.J., 1990. The petrogenesis of the Kirwan basalts of Dronning Maud Land, Antarctica. *Journal of Petrology* 31, 341–369.

- Harris, C., Johnstone, W.P., Phillips, D., 2002. Petrogenesis of the Mesozoic Sistejell syenite intrusion, Dronning Maud Land, Antarctica and surrounding low- $\delta^{18}\text{O}$ lavas. *South African Journal of Geology* 105, 205–226.
- Hourigan, J.K., Reiners, P.W., Brandon, M.T., 2005. U-Th zonation-dependent alpha-ejection in (U-Th)/He chronometry. *Geochimica et Cosmochimica Acta* 69, 3349–3365.
- Hurford, A.J., Green, P.F., 1983. The zeta age calibration of fission-track dating. *Chemical Geology* 41, 285–317.
- Ingólfsson, Ó., 2004. Quaternary glacial and climate history of Antarctica. *Developments in Quaternary Sciences* 2, 3–43.
- Isbell, J.L., 1999. The Kukri Erosion Surface; a reassessment of its relationship to rocks of the Beacon Supergroup in the central Transantarctic Mountains, Antarctica. *Antarctic Science* 11, 228–238.
- Jacobs, J., Lisker, F., 1999. Post Permian tectono-thermal evolution of western Dronning Maud Land, East Antarctica: an apatite fission-track approach. *Antarctic Science* 11, 451–460.
- Jacobs, J., Thomas, R.J., 2004. Himalayan-type indenter-escape tectonics model for the southern part of the late Neoproterozoic–early Paleozoic East African–Antarctic orogen. *Geology* 32, 721–724.
- Jacobs, J., Hejl, E., Wagner, G.A., Weber, K., 1992. Apatite fission track evidence for contrasting thermal and uplift histories of metamorphic basement blocks in western Dronning Maud Land. *Recent Progress in Antarctic Earth Science* 323–330.
- Jacobs, J., Thomas, R.J., Weber, K., 1993. Accretion and indentation tectonics at the southern edge of the Kaapvaal craton during the Kibaran (Grenville) orogeny. *Geology* 21, 203–206.
- Jacobs, J., Ahrendt, H., Kreutzer, H., Weber, K., 1995. K–Ar, 40Ar–39Ar and apatite fission-track evidence for Neoproterozoic and Mesozoic basement rejuvenation events in the Heimefrontfjella and Mannefallknusane (East Antarctica). *Precambrian Research* 75, 251–262.
- Jacobs, J., Bauer, W., Spaeth, G., Thomas, R.J., Weber, K., 1996a. Lithology and structure of the Grenville-aged (≈ 1.1 Ga) basement of Heimefrontfjella (East Antarctica). *International Journal of Earth Sciences* 85, 800–821.
- Jacobs, J., Kaul, N., Weber, K., 1996b. The history of denudation and resedimentation at the continental margin of western Dronning Maud Land, Antarctica, during break-up of Gondwana. *Geological Society, London, Special Publications* 108, 191–199.
- Jacobs, J., Fanning, C.M., Henjes-Kunst, F., Olesch, M., Paech, H.J., 1998. Continuation of the Mozambique Belt into East Antarctica: Grenville-age metamorphism and polyphase Pan-African high-grade events in central Dronning Maud Land. *The Journal of Geology* 106, 385–406.
- Jacobs, J., Bauer, W., Fanning, C.M., 2003a. Late Neoproterozoic/Early Palaeozoic events in central Dronning Maud Land and significance for the southern extension of the East African Orogen into East Antarctica. *Precambrian Research* 126, 27–53.
- Jacobs, J., Bauer, W., Fanning, C.M., 2003b. New age constraints for Grenville-age metamorphism in western central Dronning Maud Land (East Antarctica), and implications for the palaeogeography of Kalahari in Rodinia. *International Journal of Earth Sciences* 92, 301–315.
- Jacobs, J., Klemm, R., Fanning, C.M., Bauer, W., Colombo, F., 2003c. Extensional collapse of the late Neoproterozoic–early Palaeozoic East African–Antarctic Orogen in central Dronning Maud Land, East Antarctica. *Geological Society, London, Special Publications* 206, 271–287.
- Jacobs, J., Pisarevsky, S., Thomas, R.J., Becker, T., 2008. The Kalahari Craton during the assembly and dispersal of Rodinia. *Precambrian Research* 160, 142–158.
- Jenkyns, H.C., Schouten-Huibers, L., Schouten, S., Sinninghe Damsté, J.S., 2012. Warm Middle Jurassic–Early Cretaceous high-latitude sea-surface temperatures from the Southern Ocean. *Climate of the Past* 8, 215–226.
- Jourdan, F., Féraud, G., Bertrand, H., Watkeys, M.K., Renne, P.R., 2007. Distinct brief major events in the Karoo large igneous province clarified by new 40Ar/39Ar ages on the Lesotho basalts. *Lithos* 98, 195–209.
- Juckes, L.M., 1972. The Geology of North-eastern Heimefrontfjella, Dronning Maud Land. *British Antarctic Survey*.
- Kennett, J.P., Barker, P.F., 1990. Latest Cretaceous to Cenozoic climate and oceanographic developments in the Weddell Sea, Antarctica: an ocean-drilling perspective. *Proceeding of the Ocean Drilling Program, Scientific Results* 113, 937–960.
- Ketcham, R.A., 2016. Hefty, version 1.9.1. Apatite to Zircon, Inc. and Richard Ketcham.
- Ketcham, R.A., Carter, A., Donelick, R.A., Barbarand, J., Hurford, A.J., 2007a. Improved measurement of fission-track annealing in apatite using c-axis projection. *American Mineralogist* 92, 789–798.
- Ketcham, R.A., Carter, A., Donelick, R.A., Barbarand, J., Hurford, A.J., 2007b. Improved modeling of fission-track annealing in apatite. *American Mineralogist* 92, 799–810.
- König, M., Jokat, W., 2006. The Mesozoic breakup of the Weddell Sea. *Journal of Geophysical Research - Solid Earth* 111.
- Lawver, L.A., Royer, J.-Y., Sandwell, D.T., Scotese, C.R., 1991. Evolution of the Antarctic continental margins. In: Thomson, M.R.A., Crame, A., Tomson, J.W. (Eds.), *Geological Evolution of Antarctica*. Cambridge University Press, pp. 533–539.
- Leinweber, V.T., Jokat, W., 2012. The Jurassic history of the Africa–Antarctica corridor – new constraints from magnetic data on the conjugate continental margins. *Tectonophysics* 530–531, 87–101.
- Lindström, S., 1995a. Early Late Permian palynostratigraphy and palaeo-biogeography of Vestfjella, Dronning Maud Land, Antarctica. *Review of Palaeobotany and Palynology* 86, 157–173.
- Lindström, S., 1995b. Early Permian palynostratigraphy of the northern Heimefrontfjella mountain-range, Dronning Maud Land, Antarctica. *Review of Palaeobotany and Palynology* 89, 359–415.
- Luttinen, A.V., Furnes, H., 2000. Flood basalts of Vestfjella: Jurassic magmatism across an Archaean–Proterozoic lithospheric boundary in Dronning Maud Land, Antarctica. *Journal of Petrology* 41, 1271–1305.
- Luttinen, A.V., Siivola, J.U., 1997. Geochemical characteristics of Mesozoic lavas and dikes from Vestfjella, Dronning Maud Land: recognition of three distinct chemical types. *The Antarctic Region: Geological Evolution and Processes. Terra Antarctica Publications*, Siena, Italy, pp. 495–503.
- Luttinen, A.V., Rämö, O.T., Huhma, H., 1998. Neodymium and strontium isotopic and trace element composition of a Mesozoic CFB suite from Dronning Maud Land, Antarctica: implications for lithosphere and asthenosphere contributions to Karoo magmatism. *Geochimica et Cosmochimica Acta* 62, 2701–2714.
- Luttinen, A.V., Zhang, X., Folland, K.A., 2002. 159 Ma Kfajakebeinet lamproites (Dronning Maud Land, Antarctica) and their implications for Gondwana breakup processes. *Geological Magazine* 139, 525–539.
- Luttinen, A.V., Leat, P.T., Furnes, H., 2010. Björnnutane and Sembberget basalt lavas and the geochemical provinciality of Karoo magmatism in western Dronning Maud Land, Antarctica. *Journal of Volcanology and Geothermal Research* 198, 1–18.
- Luttinen, A.V., Heinonen, J.S., Kurhila, M., Jourdan, F., Mänttari, I., Vuori, S.K., Huhma, H., 2015. Depleted mantle-sourced CFB magmatism in the Jurassic Africa–Antarctica rift: petrology and 40Ar/39Ar and U/Pb chronology of the Vestfjella Dyke Swarm, Dronning Maud Land, Antarctica. *Journal of Petrology* 56, 919–952.
- Marshall, H.R., Hawkesworth, C.J., Storey, C.D., Dhuime, B., Leat, P.T., Meyer, H.-P., Tamm-Buckle, S., 2010. The Annandagstoppane Granite, East Antarctica: evidence for Archaean intracrustal recycling in the Kaapvaal–Grunehogna craton from zircon O and Hf isotopes. *Journal of Petrology* 51, 2277–2301.
- Marshall, H.R., Hawkesworth, C.J., Leat, P.T., 2013. Mesoproterozoic subduction under the eastern edge of the Kalahari–Grunehogna Craton preceding Rodinia assembly: the Ritscherflya detrital zircon record, Ahlmannryggen (Dronning Maud Land, Antarctica). *Precambrian Research* 236, 31–45.
- Martin, A.K., Hartnady, C.J.H., 1986. Plate tectonic development of the South West Indian Ocean: a revised reconstruction of East Antarctica and Africa. *Journal of Geophysical Research* 91, 4767–4786.
- McKelvey, B.C., Webb, P.N., Kohn, B.P., 1977. Stratigraphy of the Taylor and lower Victoria Groups (Beacon Supergroup) between the Mackay Glacier and Boomerang Range, Antarctica. *New Zealand Journal of Geology and Geophysics* 20, 813–863.
- Meier, S., 1999. Paleozoic and Mesozoic tectono-thermal history of central Dronning Maud Land, East Antarctica – evidence from fission-track thermochronology. *Berichte zur Polarforschung (Reports on Polar Research)* 337.
- Meier, S., Jacobs, J., Olesch, M., 2004. Tectono-thermal evolution of Central Dronning Maud Land, East Antarctica, from Mid-Palaeozoic to Cenozoic Times: zircon and apatite fission-track data from the Conradgebirge and Östliche Petermannkette. *Geologisches Jahrbuch Reihe B* 96, 423–448.
- Moyes, A.B., Barton, J.M., Groenewald, P.B., 1993. Late Proterozoic to Early Palaeozoic tectonism in Dronning Maud Land, Antarctica: supercontinental fragmentation and amalgamation. *Journal of the Geological Society* 150, 833–842.
- Näslund, J.-O., 2001. Landscape development in western and central Dronning Maud Land, East Antarctica. *Antarctic Science* 13, 302–311.
- Negi, J.G., Agrawal, P.K., Pandey, O.P., Singh, A.P., 1993. A possible K-T boundary bolide impact site offshore near Bombay and triggering of rapid Deccan volcanism. *Physics of the Earth and Planetary Interiors* 76, 189–197.
- Olaussen, S., 1985. Sedimentological research in northwestern part of Dronning Maud Land. *Report of the Norwegian Antarctic Research Expedition (NARE)* 22, pp. 75–88.
- Owada, M., Baba, S., Laufer, A.L., Elvevold, S., Shiraiishi, K., Jacobs, J., 2003. Geology of eastern Muhlig-Hofmannfjella and Filchnerfjella in Dronning Maud Land, East Antarctica; a preliminary report of a Japan–Norway–Germany joint geological investigation. *Polar Geoscience* 16, 108–136.
- Pauly, J., Marshall, H.R., Meyer, H.-P., Chatterjee, N., Montealeone, B., 2016. Prolonged Ediacaran–Cambrian metamorphic history and short-lived high-pressure granulite-facies metamorphism in the H.U. Sverdrupfjella, Dronning Maud Land (East Antarctica): evidence for continental collision during Gondwana assembly. *Journal of Petrology* 57, 185–228.
- Perritt, S.H., 2001. The Ahlmannryggen Group, Western Dronning Maud Land, Antarctica. p. 231 (Department of Geology PhD).
- Plumstead, E.P., 1975. A New Assemblage of Plant Fossils From Milorgfjella, Dronning Maud Land. *British Antarctic Survey*.
- Poole, I., Cantrill, D., Utescher, T., 2005. A multi-proxy approach to determine Antarctic terrestrial palaeoclimate during the Late Cretaceous and Early Tertiary. *Palaeogeography, Palaeoclimatology, Palaeoecology* 222, 95–121.8.
- Powell, C.M., Roots, S.R., Veevers, J.J., 1988. Pre-breakup continental extension in East Gondwanaland and the early opening of the eastern Indian Ocean. *Tectonophysics* 155, 261–283.
- Reiners, P.W., Farley, K.A., 2001. Influence of crystal size on apatite (U–Th)/He thermochronology: an example from the Bighorn Mountains, Wyoming. *Earth and Planetary Science Letters* 188, 413–420.
- Reiners, P.W., Farley, K.A., Hickey, H.J., 2002. He diffusion and (U–Th)/He thermochronometry of zircon: initial results from Fish Canyon Tuff and Gold Butte. *Tectonophysics* 349, 297–308.
- Riedel, S., Jokat, W., Steinhage, D., 2012. Mapping tectonic provinces with airborne gravity and radar data in Dronning Maud Land, East Antarctica. *Geophysical Journal International* 189, 414–427.
- Riley, T.R., Knight, K.B., 2001. Age of pre-break-up Gondwana magmatism. *Antarctic Science* 13, 99–110.
- Riley, T.R., Millar, I.L., Watkeys, M.K., Curtis, M.L., Leat, P.T., Klausen, M.B., Fanning, C.M., 2004. U–Pb zircon (SHRIMP) ages for the Lebombo rhyolites, South Africa: refining the duration of Karoo volcanism. *Journal of the Geological Society* 161, 547–550.

- Riley, T.R., Leat, P.T., Curtis, M.L., Millar, I.L., Duncan, R.A., Fazel, A., 2005. Early–Middle Jurassic dolerite dykes from western Dronning Maud Land (Antarctica): identifying mantle sources in the Karoo Large Igneous Province. *Journal of Petrology* 46, 1489–1524.
- Roeser, H.A., Fritsch, J., Hinz, K., 1996. The development of the crust off Dronning Maud Land, East Antarctica. Geological Society, London, Special Publications 108, 243–264.
- Shuster, D.L., Flowers, R.M., Farley, K.A., 2006. The influence of natural radiation damage on helium diffusion kinetics in apatite. *Earth and Planetary Science Letters* 249, 148–161.
- Smith, A.G., Hallam, A., 1970. The fit of the southern continents. *Nature* 225, 139–144.
- Spaeth, G., 2009. Mesozoic hypabyssic mafic intrusions and basalt flows in the Heimefrontfjella (East Antarctica). *Polarforschung* 79, 43–45.
- Steckler, M.S., Omar, G.I., Karner, G.D., Kohn, B.P., 1993. Pattern of hydrothermal circulation within the Newark basin from fission-track analysis. *Geology* 21, 735–738.
- Stockli, D.F., Farley, K.A., Dumitru, T.A., 2000. Calibration of the apatite (U–Th)/He thermometer on an exhumed fault block, White Mountains, California. *Geology* 28, 983–986.
- Storey, B.C., 1995. The role of mantle plumes in continental breakup: case histories from Gondwanaland. *Nature* 377, 301–308.
- Svensen, H., Corfu, F., Polteau, S., Hammer, Ø., Planke, S., 2012. Rapid magma emplacement in the Karoo Large Igneous Province. *Earth and Planetary Science Letters* 325–326, 1–9.
- Thomas, R.J., Agenbacht, A.L.D., Cornell, D.H., Moore, J.M., 1994. The Kibaran of southern Africa: tectonic evolution and metallogeny. *Ore Geology Reviews* 9, 131–160.
- Thorn, V.C., DeConto, R., 2006. Antarctic climate at the Eocene/Oligocene boundary – climate model sensitivity to high latitude vegetation type and comparisons with the palaeobotanical record. *Palaeogeography, Palaeoclimatology, Palaeoecology* 231, 134–157.
- Wareham, C.D., Pankhurst, R.J., Thomas, R.J., Storey, B.C., Grantham, G.H., Jacobs, J., Eglinton, B.M., 1998. Pb, Nd, and Sr isotope mapping of Grenville-age crustal provinces in Rodinia. *The Journal of Geology* 106, 647–660.
- White, R., McKenzie, D., 1989. Magmatism at rift zones: the generation of volcanic continental margins and flood basalts. *Journal of Geophysical Research - Solid Earth* 94, 7685–7729.
- Wildman, M., Brown, R., Watkins, R., Carter, A., Gleadow, A., Summerfield, M., 2015. Post break-up tectonic inversion across the southwestern cape of South Africa: new insights from apatite and zircon fission track thermochronometry. *Tectonophysics* 654, 30–55.
- Wildman, M., Brown, R., Beucher, R., Persano, C., Stuart, F., Gallagher, K., Schwanethal, J., Carter, A., 2016. The chronology and tectonic style of landscape evolution along the elevated Atlantic continental margin of South Africa resolved by joint apatite fission track and (U–Th–Sm)/He thermochronology. *Tectonics* 35, 511–545.
- Wildman, M., Brown, R., Persano, C., Beucher, R., Stuart, F.M., Mackintosh, V., Gallagher, K., Schwanethal, J., Carter, A., 2017. Contrasting Mesozoic evolution across the boundary between on and off craton regions of the South African plateau inferred from apatite fission track and (U–Th–Sm)/He thermochronology. *Journal of Geophysical Research - Solid Earth* 122, 1517–1547.
- Wilson, K.M., Pollard, D., Hay, W.W., Thompson, S.L., Wold, C.N., 1994. General circulation model simulations of Triassic climates: preliminary results. *Pangea: Paleoclimate, Tectonics, and Sedimentation During Accretion, Zenith, and Breakup of a Supercontinent* 288, 91–116.
- Wolmarans, L., Kent, L., 1982. Geological Investigations in Western Dronning Maud Land, Antarctica, a Synthesis. South African Scientific Committee for Antarctic Research.
- Yumoto, M., Ogata, T., Matsuoka, N., Matsumoto, E., 2006. Riverbank freeze-thaw erosion along a small mountain stream, Nikko volcanic area, central Japan. *Permafrost and Periglacial Processes* 17, 325–339.
- Zhang, X., Luttinen, A.V., Elliot, D.H., Larsson, K., Foland, K.A., 2003. Early stages of Gondwana breakup: the ⁴⁰Ar/³⁹Ar geochronology of Jurassic basaltic rocks from western Dronning Maud Land, Antarctica, and implications for the timing of magmatic and hydrothermal events. *Journal of Geophysical Research - Solid Earth* 108.